EFEFCTS OF COLLAGEN ORIENTATION ON THE MEDIUM-TERM FATIGUE RESPONSE OF HEART VALVE BIOMATERIALS

by

Tiffany Leigh Sellaro

BS, The George Washington University, 1999

Submitted to the Graduate Faculty of

School of Engineering in partial fulfillment

of the requirements for the degree of

Master of Science

University of Pittsburgh

2003

UNIVERSITY OF PITTSBURGH

SCHOOL OF ENGINEERING

This thesis was presented

by

Tiffany Leigh Sellaro

It was defended on

April 11, 2003

and approved by

Dr. Lars Gilbertson, Assistant Professor, Department of Bioengineering

Dr. William Slaughter, Associate, Professor, Department of Mechanical Engineering

Thesis Advisor: Dr. Michael Sacks, Associate Professor, Department of Bioengineering

ABSTRACT

EFFECTS OF COLLAGEN ORIENTATION ON THE MEDIUM-TERM FATIGUE RESPONSE OF HEART VALVE BIOMATERIALS

Tiffany Leigh Sellaro, MS

University of Pittsburgh, 2003

Worldwide 275,000 diseased heart valves are replaced annually and approximately 50% are bioprosthetic heart valves (BHV). BHV are fabricated from biologically derived tissues chemically modified to reduce immunogenecity and improve durability. BHV are nonviable, non-renewing biomaterials that undergo progressive degenerative changes in-vivo resulting in durability issues, which can be due to both calcific and non-calcific mechanisms. In-vitro durability testing of intact valves up to $200x10^6$ cycles is used to assess BHV durability. In-vitro durability testing confounds characterization and modeling of fatigue. Thus there is a need for elucidation of the underlying mechanisms in the BHV response to repeated cyclic loading (RCL), independent of BHV design.

In this study, the effects of collagen orientation on the medium-term (up to $50x10^6$ cycles) BHV RCL response was investigated. Glutaraldehyde treated bovine pericardium were subjected to cyclic tensile loading to stress levels of 500±50 kPa at a frequency of 22 Hz. Two specimen groups were examined, with the preferred collagen fiber direction parallel (PD) and perpendicular (XD) to the direction of loading. Small angle light scattering (SALS) was used to assess the degree of fiber reorientation of the BHV collagenous network after 0 and $50x10^6$ cycles. After 0, $20x10^6$ and $50x10^6$ cycles, specimens were subjected to biaxial mechanical testing and Fourier transform IR spectroscopy (FT-IR) was performed to assess molecular level changes to collagen . In addition, and the collagen fiber crimp period was also measured.

Substantial permanent set effects were observed in both groups. In the perpendicular group, the areal stretch, which is a measure of overall tissue compliance, increased significantly while in the parallel group the areal stretch decreased significantly after $50x10^6$ cycles. After $50x10^6$ cycles, SALS measurements revealed that in the perpendicular group, the collagenous fibers became less aligned and in the parallel group, the collagen fibers became more highly aligned. The only significant changes in collagen crimp were an increase in collage crimp period from 23.46 1.39 m (at 0 cycles) to 28.14 0.84 m after $20x10^6$ cycles in the parallel group. FT-IR spectra indicated that RCL of both of the groups lead to collagen conformational changes and early denaturation after $20x10^6$ cycles.

The results of this study suggest that 1) collagen orientation plays a critical role in BHV fatigue response, and 2) chemical fixation technologies that allow greater fiber mobility under functional stresses yet without permanent set effects may yield more durable materials.

ACKNOWLEDGMENTS

I would like to thank my committee members, Dr. Lars Gilbertson and Dr. William Slaughter, for their expert advice, helpful insights and encouragement. I would also like to thank Dr. Michael Scott of Edwards Lifesciences for his assistance in my research. In addition, I would like to thank Dr. Simon Watkins and Sean Alberts of the University of Pittsburgh Center for Biological Imaging for their assistance with microscopy.

I would like to thank all the members of the Engineered Tissue Mechanics Lab for the continuous support and encouragement throughout my years here at the University of Pittsburgh. In particular, I would to thank Thanh Lam and George Engelmayr for being there as a sounding board. I would also like to thank John Kompel of the Department of Orthopeadic Surgery for his moral support and assistance in the preparation of my presentation. I would also like to thank those unsung heroines in the BIOE department, Lynette Spataro and Joan Williamson, for always being there.

I would like to thank my parents, Louis and Carole Sellaro, and my sister Ashley, for their undying love and support. My parents always encouraged me to strive for excellence and to be the very best that I can be. My family was always there for me rain or shine, unconditionally, and for that I am truly indebted.

Finally, I would like to thank my thesis advisor and professional mentor, Dr. Michael S. Sacks. Through his hard work and dedication to scholarly research in the field of soft tissue biomechanics, he provided me with the resources necessary to complete my thesis. Moreover, I would like to thank Dr. Sacks for his guidance throughout my research projects. I am hopeful that I may perpetuate the knowledge he so generously shared to future generations of engineers.

TABLE OF CONTENTS

LIST OF TABLES

LIST OF FIGURES

1.0 INTRODUCTION

1.1 Basic Aortic Valve Anatomy

The contracting myocardium enables the heart to continuously circulate blood throughout a lifetime, while the cardiac valves ensure proper flow. The myocardium consists mostly of myocytes and capillaries that are embedded in an extensive network of connective tissue while the cardiac valves are comprised mostly of connective tissue. The valves ensure proper hemodynamic function of the heart by regulating the flow of blood into the various heart chambers. In the mammalian heart, there are four cardiac valves: the aortic and mitral valves in the left side of the heart and the pulmonary and the tricuspid valves in the right side of the heart (Figure 1). Both the mitral and aortic valves undergo greater pressure differences.

On the most basic functional level, the aortic heart valve is essentially a check-valve that prevents retrograde blood flow from the aorta back into the left ventricle (Figure 1). This seemingly simple function belies the structural complexity, elegant solid-fluid mechanical interaction, and durability necessary for normal aortic valve function [1]. For example, the aortic valve is capable of withstanding 30-40 million cycles per year, resulting in a total of ~3 billion cycles in single lifetime [2]. No valve made from non-living materials has been able to demonstrate comparable functional performance and durability.

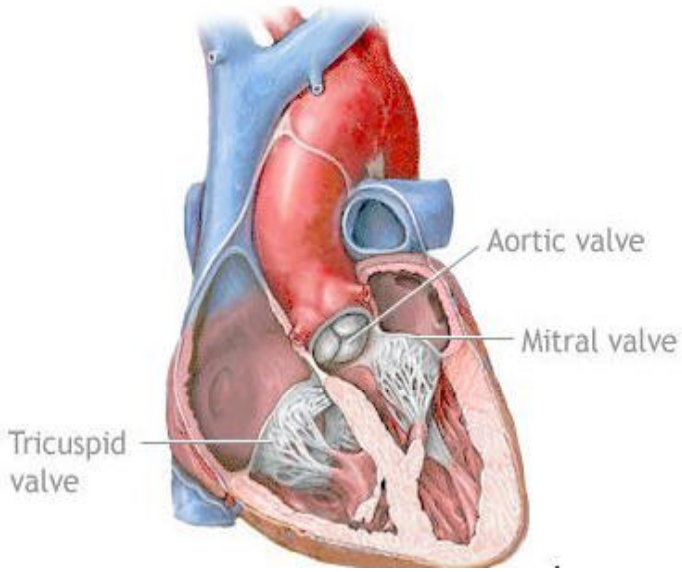

Figure 1 Schematic of the heart showing three of the four valves and their respective locations within the heart. (**http://www.chelationtherapyonline.com)**

1.2 Heart Valve Disease

Heart valve disease afflicts many people and manifests in two forms: (1) stenosis, which is a narrowing of the valve which obstructs blood flow, is the most common form of aortic valve disease, and (2) widened or scarred valves, which allows retrograde blood flow. The current method to treat aortic valve disease is to completely replace the valve. First performed successfully in 1960, surgical replacement of diseased human heart valves by valve prostheses is now commonplace and enhances survival and quality of life for many patients. Over 70,000 substitute valves are implanted in the United States and 170,000 worldwide each year. Approximately 50% are bioprosthetic heart valve (BHV) [3], which are fabricated from biologically derived tissues chemically modified to reduce immunogenecity and improve durability.

If a heart valve is congenitally defective or degenerates over time, the heart cannot pump blood as efficiently. It must work harder to maintain the same cardiac output, which causes the heart to hypertrophy and eventually fail. The degenerative process can take years and the quality of life for the patient diminishes severely. If the valve cannot be surgically repaired, the only alternative is replacement of the defective valve with an artificial or bioprosthetic valve.

When implanting a prosthetic heart valve, the surgeon must choose from many commercially available designs. Heart valve replacements are of two principal types: mechanical prostheses, which are composed entirely of synthetic materials, or biologic tissue prostheses (bioprostheses), which are composed largely of human or animal tissues that may be chemically treated, and may or may not be mounted on a stent (Figure 2c). Tissue valves include homografts / allografts (human cadaver, Figure 2b), heterografts / xenografts (chemically treated porcine aortic valve or bovine pericardial tissue), or autografts (use of patient's own pulmonary valve, thigh connective tissue, or pericardium) [4].

1.3 Mechanical Valves

Mechanical valves are very durable but their main disadvantage is the risk of blood clots (Figure 2a). Thrombus formations on the valve components can cause valve occlusion, or the thrombi can be liberated and lead to strokes or myocardial infarctions. Anticoagulation therapy using usually Coumadin, is required in mechanical heart valves because thromboembolic complications are a major cause of mortality and morbidity in patients with substitutes [5]. Patients must be closely monitored and a delicate balance must be maintained: inadequate anticoagulation leads to blood clotting, while excess therapy can cause dangerous internal bleeding or blood loss from minor injury.

(a) (b) (c)

Figure 2 Mechanical valve (a) allograft replacement valve (b) porcine aortic heart valve that has been chemically treated with glutaraldehyde (c).
http://www.chelationtherapyonline.com

1.4 Bioprosthetic Valves (BHV)

Bioprostheses are hybrid structures comprised of biologically derived (cuspal) tissue and synthetic parts. The two synthetic parts are the stent supports, which are typically comprised of three struts onto which the tissue valves are mounted, and a very thin polyester mesh sewing cuff that is usually placed around the outside of the valve. Both the stent and sewing cuff facilitate surgical implantation and permit valve use in either the semilunar (aortic/pulmonary) or atrioventricular (mitral/tricuspid) valve sites. Depending on the model, the stent will vary in structural design, flexibility and composition (metal or plastic).

The two most commonly used biologically derived materials are porcine aortic valve and bovine pericardium. If the tissue is animal-derived, it will be treated with a chemical before implantation. The most common treatment is glutaraldehyde (glut), which is a dialdehyde ($CHO[CH_2]_3CHO$). Glut fixed valves were first implanted in 1967 after it was determined that glutaraldehyde stabilized collagenous biomaterials [6].

Glutaraldehyde fixation protects the tissue against enzymatic degradation, sterilizes pathogenic agents and reduces immunogenic responses. Glutaraldehyde forms complex, degradation-resistant, intermolecular cross-links with predominantly collagen.

Glutaraldeyde-preserved trileaflet bovine pericardial prostheses were first introduced in 1977 [7]. The pericardium is a conical fibro-serous sac, in which the heart and the roots of the great vessels are contained. Although the pericardium is usually described as a single sac, an examination of its structure shows that it consists essentially of two sacs intimately connected with one another, but totally different in structure. The outer sac, known as the fibrous pericardium**,** consists of fibrous tissue. The fibrous pericardium forms a flask-shaped bag, the neck of which is closed by its fusion with the external coats of the great vessels, while its base is attached to the central tendon and to the muscular fibers of the left side of the diaphragm. The inner sac, or serous pericardium**,** is a delicate membrane that lies within the fibrous sac and lines its walls; it therefore consists of a visceral and a parietal portion**.** The visceral portion, or epicardium, covers the heart and the great vessels, and from the latter is continuous with the parietal layer, which lines the fibrous pericardium. The parietal layer is used in the construction of the bovine pericardial valves. Parietal pericardium has (1) a smooth serosal layer; (2) the fibrosa, which spans almost the entire thickness and contains collagen elastin, nerves, blood vessels and lymphatics; (3) a rough epipericardial connective tissue. Pericardial valves are constructed with the epipericardial side facing the inflow, which is thought to keep the surface “clean” thereby minimizing thrombogenic reactions.

Bovine pericardial valves are comprised of sheets of treated calf pericardium that are molded and sewn to a stent. This forms three cusps similar in shape to the natural aortic valves. Bovine pericardium is comprised of collagen type 1 only [6]. The collagen fibers in pericardial tissue are not as aligned as porcine valve fibrosa [8].

While the pericardial tissue is predominantly homogenous in composition, comprised mainly of collagen Type I and elastin, the aortic valve has three distinct layers: (1) the ventricularis, predominantly collagenous with some elastic fibers that face the inflow surface; (2) the centrally located spongiosa, composed of loosely arranged collagen and abundant proteoglycans; and (3) the fibrosa, composed of densely packed collagen, facing the outflow surface [6]. The porcine aortic valve contains type I and III collagen [6].

1.5 Porcine and Pericardial Valve Complications

Tissue valves are hemodynamically superior to mechanical valves and have a low incidence of thrombogenicity, requiring little or no anticoagulant therapy [4]. Although bioprostheses offer a promising alternative to mechanical prostheses, bioprostheses are nonviable, non-renewing biomaterials that undergo progressive degenerative changes during function.

Durability limitations related to the changes the valves undergo while *in vivo* have been the major impediment to their long-term success [9] [10] [11]. The durability of bioprosthetic heart valves is approximately 10-15 years in an older adult and an even shorter lifetime in children, adolescents and younger adults (<60 years of age) [12]. Progressive structural valve deterioration is the major cause of bioprosthetic valve failure in the most widely used bioprostheses, which is stent-mounted glutaraldehyde-preserved bovine pericardium or porcine aortic valves [13] [14]. Bioprosthetic heart valve degeneration, characterized by extracellular matrix deterioration, remodeling, and calcification, is an important clinical problem accounting for thousands of surgeries annually.

The previous dogma of BHV failure processes was that calcification alone in BHV resulted in failure. However, several studies have recently shown that collagen fiber

damage in BHV can occur in spatially distinct areas from calcification in clinically explanted BHV [15] [16]. Thus, structural failure can occur either isolated due to non-calcific tearing or synergistically with cuspal mineralization (with or without cuspal tearing) (Figure 3).

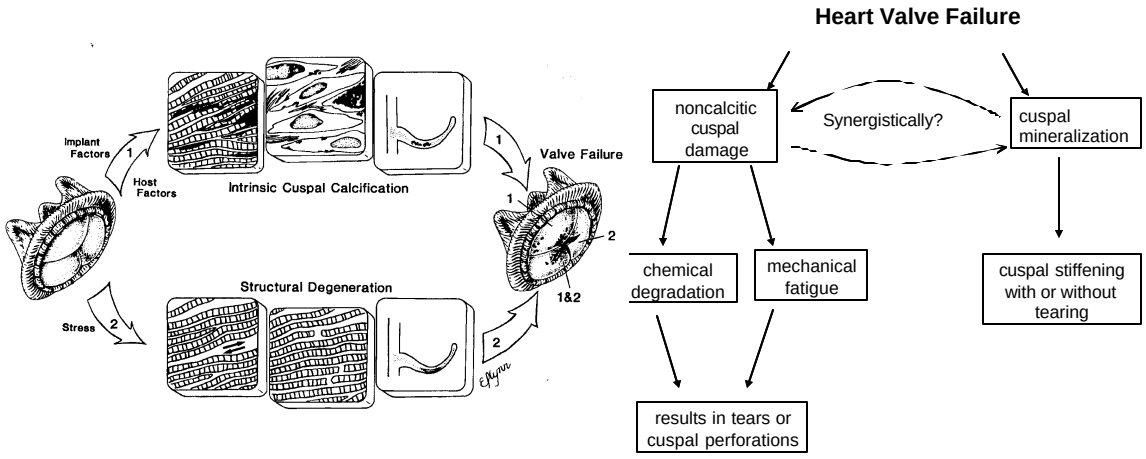

Figure 3 The schematic on the left portrays the different pathways leading to heart valve failure while the chart delineates the pathway. (Schoen, F., Levy, B. (1999) Tissue heart valves: Current challenges and future research perspectives. Journal of Biomedical Materials Research, Vol 47, 439-465)

Mechanical damage may be mediated by stress concentrations within the cuspal tissue induced by calcification, by structural damage induced by calcific deposits, or by direct fatigue effects (i.e., unrelated to calcification). Mechanical deformation seems to potentiate mineralization, but the details of the process are unclear. Generally, in-vivo cyclic mechanical stresses are thought to initiate calcification by causing structural disintegration of the valvular tissue, enabling multiple pathways of calcification. Tissue buckling has been observed on the surface of heart valves and is implicated in the failure process by both in-vivo and by in-vitro evidence [17].

Biomechanical processes such as tearing or fatigue, independent of calcification, and both cyclic bending strains and high membrane stresses have been implicated in leaflet failure [15, 17]. While collagen structure degradation is not a strict prerequisite for calcification, these andother studies have demonstrated that maintaining tissue structural integrity is a prime factor in inhibiting calcification and extending durability.

1.6 Collagenous Soft Tissues

Collagen is the most widespread protein present in all vertebrate species and has been estimated to account for about 30% of the body protein in mammals [18]. In general terms, collagenous tissues consist of collagen fibrils embedded in an amorphous gel-like matrix composed of proteoglycans and water. To date, at least 19 distinct collagen types have been characterized [19] with at least 30 distinct polypeptide chains [20]. All collagens share the triple helix macrostructure and only the macroscopic organization is varied to meet the requirements of a specific application.

Fibrous collagen is the primary structural element found in mammalian extracellular matices. Collagen types I-III form fibers that maintain tissue shape, transmit and dissipate loads, prevent premature mechanical failure, partition cells and tissues into functional units, act as a scaffold that supports tissue architecture and as a storage device for elastic energy [21]. Collagen type I, the major component of tendons, heart valves, and other connective tissues, is the major load bearing protein in soft tissues.

Collagen is a hierarchical structure – there exists a well-defined structure and a high degree of organization from the molecular to the macroscopic level (Figure 4) [22]. The basic building block of all collagens is a triple-helix molecule synthesized from three amino acid chains coiled into left-hand helices. The composition in the chains are the same in two and slightly different in the third. The molecule itself is a right-handed

superhelix formed by these three chains. The main part of the chain has a very regular amino acid sequence: Glycine-X-Y-Glycine-X-Y where X and Y are frequently proline, and hydroxyproline but other amino acids could be present in variable proportions. Glycine comprises about 33% of the amino acid chain while proline and hydroxyproline comprise about 15% [23].

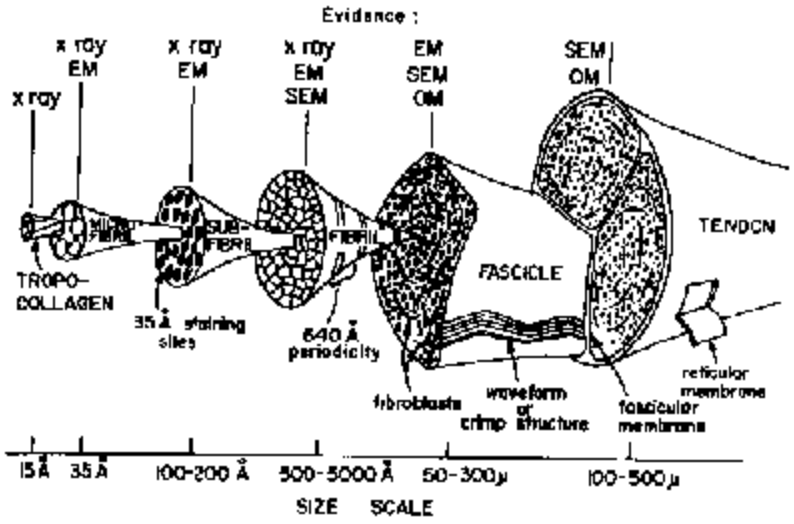

Figure 4 Hierarchical structure of the tendon [24].

This structure is made possible due to the staggered arrangement of the three chains. The staggered arrangement allows glycine, which has the smallest side chains (just H), to be present at each axial position. The presence of glycine as every third residue makes the confirmation of the helix-superassembly possible. The highly specific alignment and packing of the helix-superassembly molecules in the fibrils and the structural stability provided by the formation of intermolecular covalent crosslinks ensures the required tensile strength and elasticity seen in collagen. These chains of amino acids are uniformly 290 nm in length and form a triple helical structure called tropocollagen.

The fiber-forming collagens are all triple helices containing three α-chains, which is a trimer, with approximately 1000 amino acids. These chains lead to higher level structures either by parallel association, or in the case of type IV, forming branched three-dimensional networks (basement membranes). Figure 5 delineates the overall general pathway to construction of fibrous collagen. From this point on, all discussion will pertain to the fiber forming collagens.

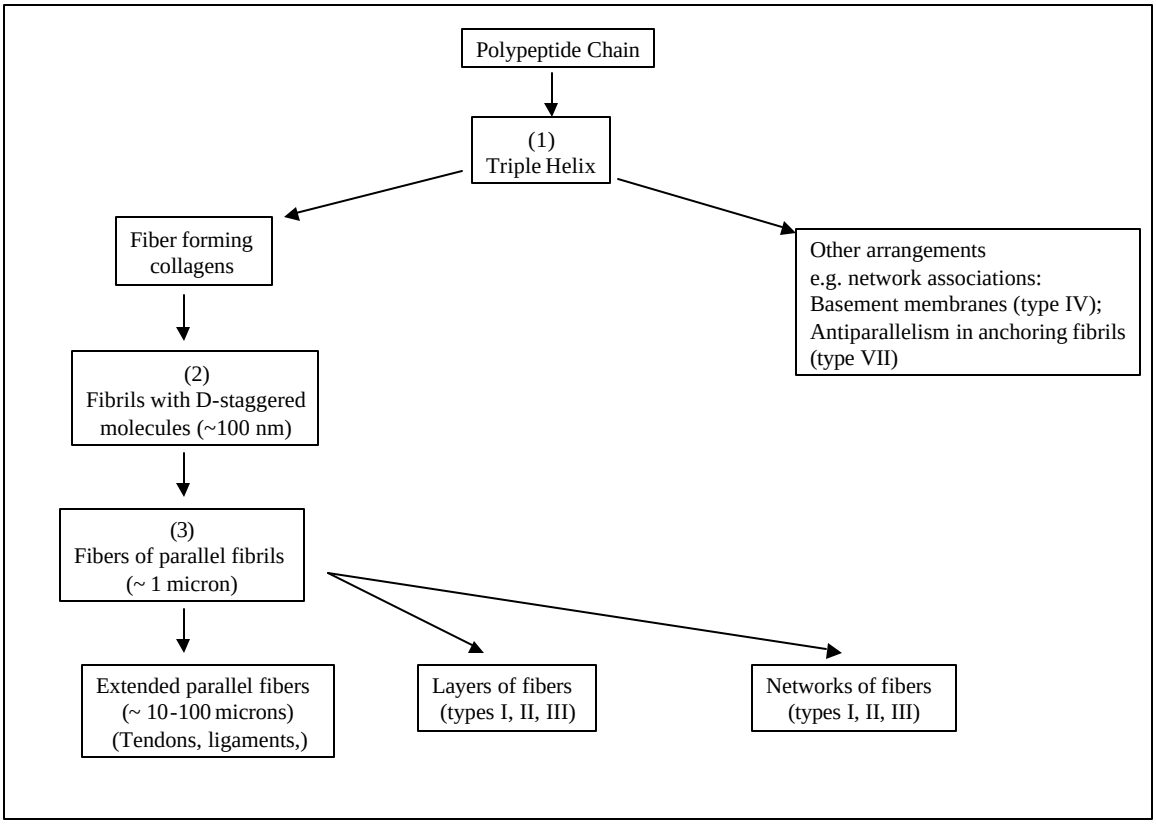

Figure 5 Flow chart depicting the overall steps in the construction of fibrous collagen.

1.6.1 Construction of Collagen

Collagen construction begins when the α-chains of pre-procollagen precursor are synthesized on ribosomes and the endoplasmic reticulum (ER) [25] as seen in Figure 6. Hydroxylation, which is the substitution of –OH group for an H atom, of the proline

residues in Y position is converted to hydroxyproline (hyp). Hydroxylation of proline secures the chains in the triple helix collagen molecule. Concurrently, lysine is converted to hydroxylysine (hyl) through hydroxylation. Hydroxylysine is needed to permit the cross-linking of the triple helices into the fibers. Glycosylation via addition of glucose and galactose are added to some of the hydroxylysine residues.

The next step is the assembly of the three alpha chains to form procollagen. Nucleation happens at the C end due to disulphide bonds [25],

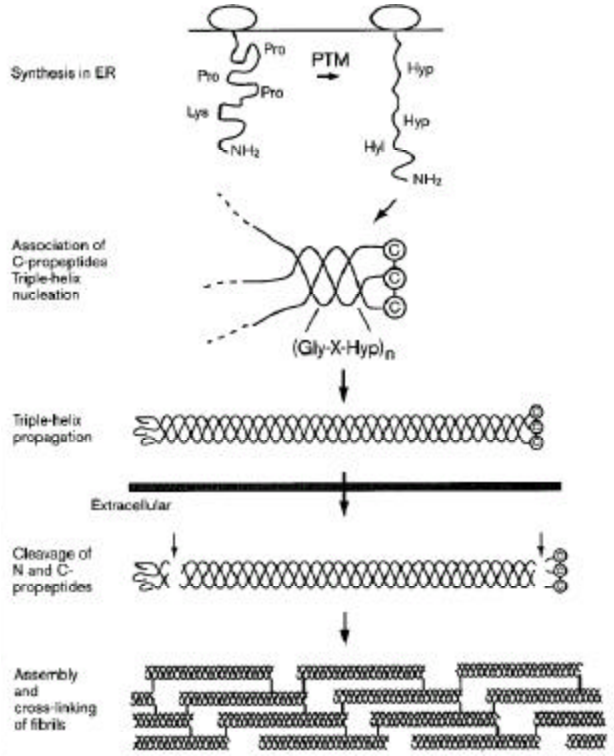

Figure 6 Folding process of a collagen trimer. **(www.cs.ucsb.edu/~isaacs/collagen.doc)**

aligning the three chains. This alignment allows the triple helix to form in a zipper-like manner giving procollagen. Procollagen is secreted by exocytosis into the extracellular space. In the extracellular space, the peptides are cleaved by procollagen peptidases and the resulting molecule is collagen.

The next stage of collagen development is normally referred to as the "crystalline structure", which is the 3-dimensionally repeating arrangement of the collagen

molecule and of its peptide subunits comprised by a fibril. X-ray diffraction is a key resource that is used to investigate the molecular packing of collagen. X-ray diffraction studies that were performed on rat tail tendon, which has well oriented and ordered fibers, revealed that there is a three dimensional crystalline organization of the collagen molecules in the fibrils [26]. It is this crystalline organization that gives rise to the supermolecular coiling. All fibrils possess the 67-nm periodicity, commonly referred to as the D-period (1/4 of the total length of the collagen molecule). Figure 7 shows several collagen molecules that are aggregated into a staggered parallel array. The linear polymers are staggered relative to one another by four D units of 268 nm and the substructure created is comprised of five microfibrils [27]. This staggering creates holes and overlap zones causes the cross striation visible in the collagen fibril under the electron microscope [28]. The periodicity when viewed under an electron microscope, is manifest as light and dark banding. The fibril diameter ranges from 10 nm to 100 nm where collagen type I fibrils are among the largest of all the fibrils (~100 nm).

Addition of further molecules occurs by axial packing in which the molecules are staggered relative to the initial molecules by one D (67 nm) intervals creates overlap and gap zones that are responsible for the periodicity of the collagen fibers, which is referred to as the Hodge and Petruska model [29].

Moving towards the macroscopic level, construction of the fiber involves lateral association and axial displacement of molecules arranged in parallel. The fibrils can aggregate either by forming larger scale parallel arrays or by forming more complicated 2- or 3- dimensional super-structures. Fiber crimp characteristics, the polarizing optically identifiable alternating dark and bright-banded extinction structure, are first observed at this stage. The dimensions of the fibers range from ~1 μm to several 100 μm. Further construction into large scale units can follow along the same two lines as seen previously on the lower dimensional units: the fiber may aggregate in a parallel fashion leading to the macroscopic tendon or give rise to woven or other more complex arrangements.

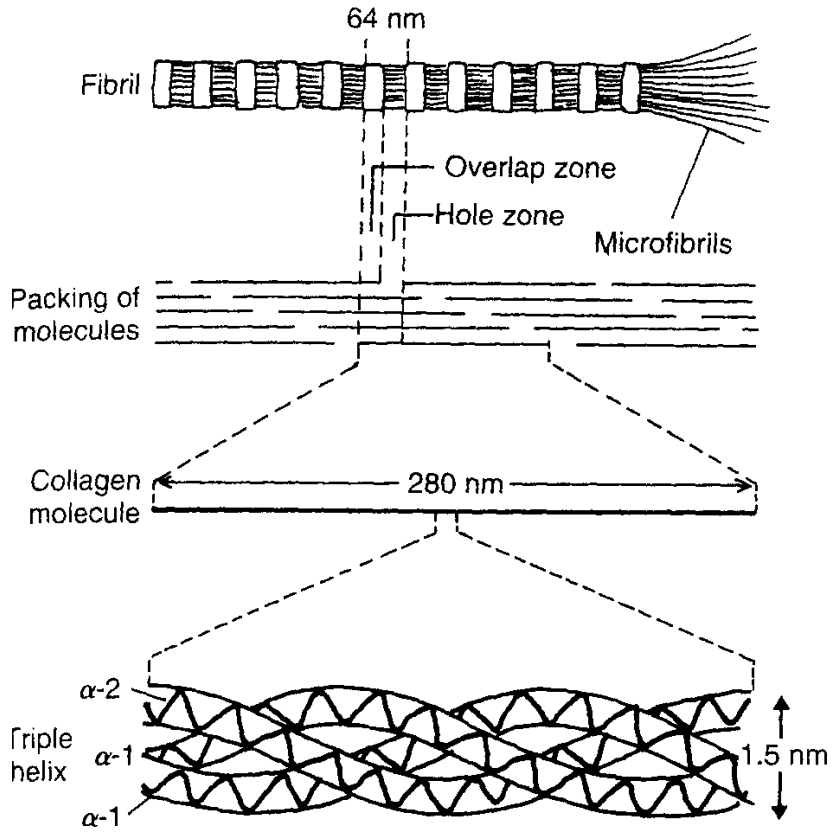

Figure 7 Schematic drawing of collagen microstructure. Several collagen molecules are aggregated into a staggered parallel array. This staggering creates holes and overlap zones causes the cross striation visible in the collagen fibril under the electron microscope. (Adapted from Prockop, D.J. et al. (1977) *Collagen diseases and the biosynthesis of collagen*. Hosp practice, Dec, 61-68.)

1.6.2 Collagen Packing Theories

There are various theories of packing that exist but exactly how the trimers, the three alpha helices, pack is not known for sure. The packing can occur in various ways [30] [28]. Early suggestions for packing are indicated in Figures 8 a & b. Packing process could determine individual trimer shape. Figure 9 shows that depending on where the trimer is added, each model can have different influences on trimer shape. Packing density of trimers could correspond to function of the fiber-natural selection and studies of function-structure of fibers would suggest this [31]. One must bear in

mind that Figure 8 is a 2D representation of packing in 3 dimensions. Figures 10 a & b give a view into in vivo nature of collagen packing [32].

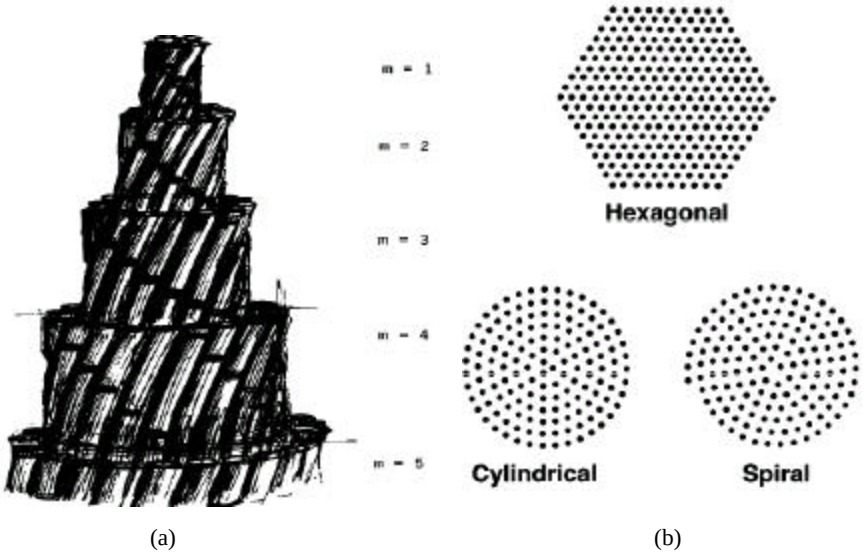

Figure 8 Galloway model of trimer packing- fiber intermediate stage (a). Early Ramachandran models of packing – axial view of fibers (b). (Ottani, V.,Raspanti, M.,Ruggeri, A.(2001). *Collagen strucutre and functional implications,* Micron, vol 32, 251-260.)

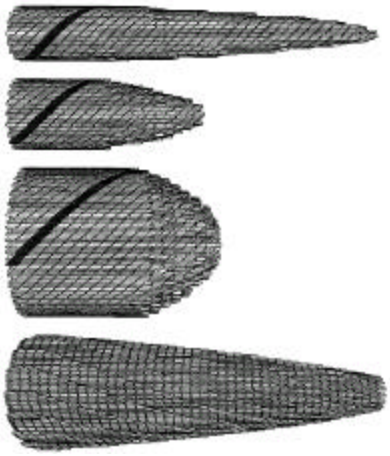

Figure 9 Depending on how trimers are added, the shape of the molecule can be greatly altered. (Ottani, V.,Raspanti, M.,Ruggeri, A.(2001). *Collagen strucutre and functional implications*, Micron, vol 32, 251-260.)

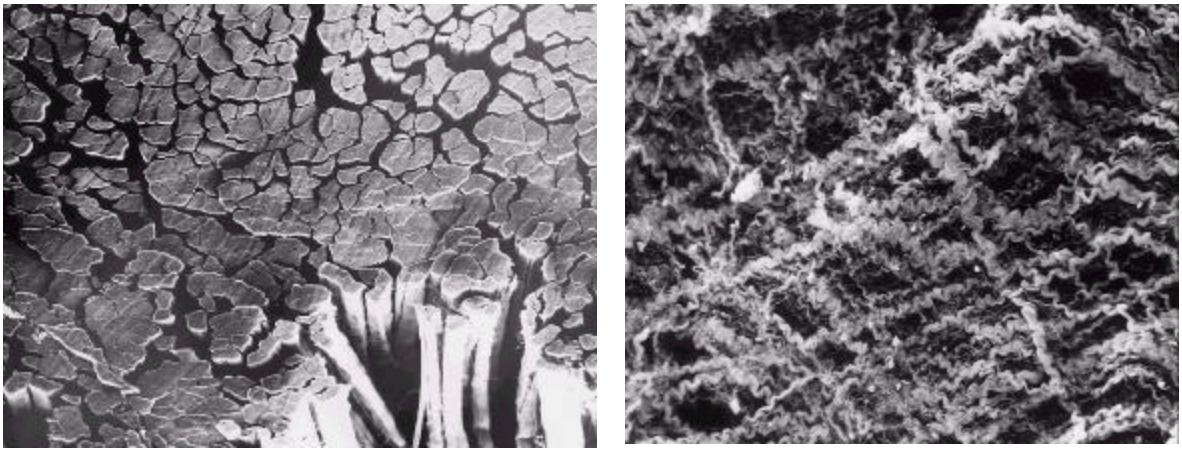

(a) (b)

Figure 10 Cross sectional view of tendon collagen fiber showing the thick, straight, tightly packed, parallel fascicles (a). Connective stroma of small intestine showing that the collagen bundles are slender and oriented in all directions (b). (Ottani, V.,Raspanti, M.,Ruggeri, A.(2001). Collagen strucutre and functional implications, Micron, vol 32, 251-260.)

1.6.3 Structure-function Relationship of Collagenous Tissues

Collagen plays a major role in specifying the form and structural integrity of the tissue. Collagen's major role in soft tissue is to transmit load to other structures and to provide internal structural support for soft tissues. This important property of collagen is due to its unique molecular conformation. In soft tissues, it is the aggregates of collagen fibrils into fibers, not the individual collagen fibrils, which allow the tissue to withstand the demands of its loading environment. The construction of the aggregates is of a paramount importance to the integrity of the tissue.

Mechanical properties of collagenous tissues can vary widely depending on the distribution of the collagen fibril sizes, the orientation of the collagen fibers, and the interactions between the collagen and the matrix constituents. Collagen's ultimate tensile strength of fibrils, in the range of 1 MPa, is directly proportional to the diameter of the fibrils [33]. Thus in loading environments that require the tissue to undergo high tensile loads, the collagens fibers will have a greater cross sectional area.

In addition to fiber diameter, there is a strong correlation between collagen fiber orientation and the functional requirements. Collagen fiber orientation and sequential reorientation to applied loads plays a paramount role in the overall tissue behavior. The collagen fiber orientation significantly influences the mechanical properties of collagen. Figure 11 is a schematic showing different fiber geometries found in collagenous networks and their corresponding stress-strain relationships. In Figure 11, in case A the fibers are perfectly aligned which correlates to a very stiff collagenous network. In case B, the fibers are slightly crimped to the same degree, which introduces a slight non-linearity in the stress-strain curve. In case C, the varying degrees of collagen fiber crimp yield a large toe-region while the random orientation of the collagen fibers contributes to the overall compliance of the tissue. Tissues tend not to have perfectly oriented fibrils because few tissues are subjected to a pure tensile loading.

Conversely, few tissues have completely random arrangements of fibrils, which would permit a tissue to withstand tensile stresses equally in all directions, because many tissues are only subjected to forces that act in specific ways. Further, if fibers were completely random, it would not be possible to achieve efficient packing of the fibers and low packing fractions lead to low stiffness [34].

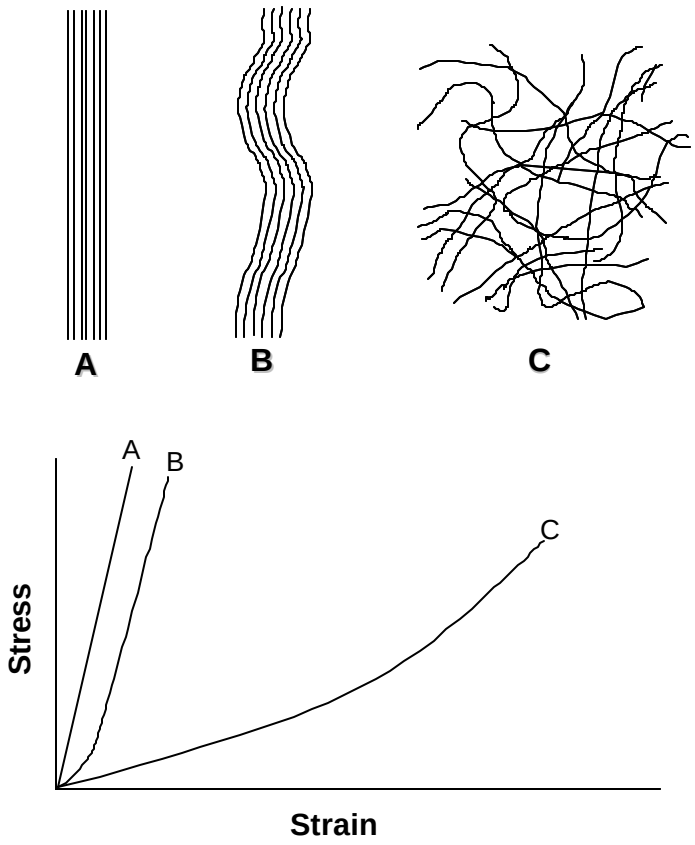

Figure 11 Typical fiber geometries in collagenous networks and resultant stress-strain behaviors. In (a), the fibers are perfectly aligned which correlates to a very stiff stress-strain response. In (b), the fibers are slightly crimped which introduces a slight non-linearity in the first portion of the curve. In (c), the varying degrees of collagen fiber crimp yield a large toe-region while the random orientation of the collagen fibers contributes to the overall compliance of the tissue. (Jeronimidis, G. et al. Composite materials. Connective Tissue Matrix, 1984, 187-245)

Fiber direction is always indicative of prevalent tensile stresses because fiber reorientation is the most efficient and selective way to optimize strength without increasing weight and metabolic costs [33]. The collagen type present in a soft tissue is often dictated by the tissue's loading environment. The loading environment also controls the architecture of the collagenous framework. Many tissues have characteristic arrangements of fibrils that have definite preferred orientations. The preferred orientations can be dynamic and may change while the tissue is performing some mechanical function. Since collagen fibrils appear to have low torsional and flexural stiffness [35], the direction in which fibrils are oriented can be identified with the direction of tensile loading. Figure 10a shows tightly packed collagen in a tendon that has the ability to handle forces along its lateral axis. There can be more than one preferred fiber orientation in a tissue. Figure 10b shows collagen fibril packing in 3 dimensions in the intestinal stroma and it is meant to handle forces in all directions.

The main mechanical function of the pericardial sac is to maintain the shape of the heart to permit normal functional output. The pericardial sac will have to vary in shape throughout life and adjust to stresses in varied directions. The role of collagen in a flat membranous structure like pericardium is to function as a tensile element [26]. This explains why the pericardium is comprised mainly of collagen Type I, which the main function of this collagen is to transmit loads.

1.6.4 Nonlinearity of Soft Tissues

A stress strain curve for most tissues may be divided into three distinct regions, each of which may be attributed in part to the different levels of structural hierarchy present in the tissue. Several theories exist that try to elucidate collagen fiber crimp and its relation to the nonlinear stress-strain curve associated with soft tissues. The governing theory in collagen fiber recruitment is described here [36] [37] [38]. In phase 1, in the absence of any load, the collagen fibers appear wavy and there exists a high degree of periodicity. In this phase, low stress is required to achieve large deformations of collagen fibers without requiring stretch of the fibers. The nonlinearity

of the toe region is due to collagen fiber recruitment (Figure 12). More specifically, it is the gradual straightening of the collagen fibers that have varying degrees of undulations [39]. As the collagen fibers begin to bear load, the fibers begin to uncrimp. In phase II, as the load is increased, the collagen fibers tend to line up in the direction of the load and begin to bear load. This correlates to an increase in stiffness due to the collagen fibers resisting the load at a given stress level. The increasing stiffness of the fiber stress-strain curve correlates with the increasing number of recruited fibers. As the load increases, the collagen fibers continue to elongate with a decrease in crimp angle in fibrils until most of the crimp is removed which is the onset of phase III. Figure 13 depicts phase I-III progression graphically.

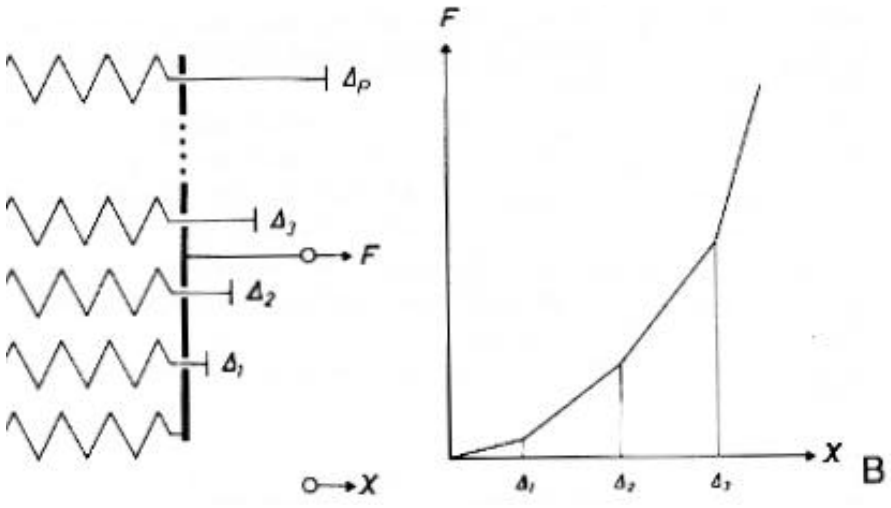

Figure 12 Model of nonlinear elasticity demonstrating progressive recruitment of individual linear components (a). Resultant nonlinear load-deformation curve (b). (Frisen, M. et al. (1969). Rheological analysis of soft collagenous tissue. Part I: theoretical considerations. J. Biomech., 2-13)

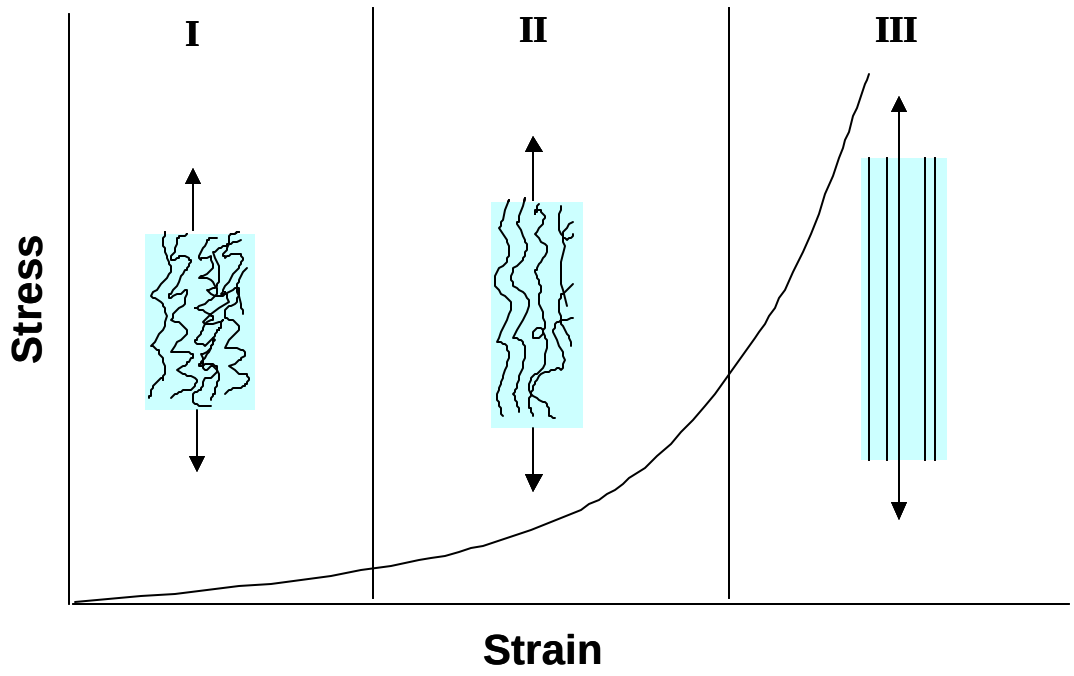

Figure 13 Schematic diagram of tensile stress-strain curve for skin showing the associated collagen fiber network and resultant nonlinear load-deformation curve. (Holzapfel, G.A. Nov 2000. Biomechanics of soft tissue. Computational Biomechanics)

1.6.5 Collagen Crimp

Crimp or periodicity is a very prominent feature associated with collagen Types I-III. When viewed under polarized light, collagen exhibits a characteristic series of light and dark bands termed an extinction pattern. Diamant et al (1972) interpreted the periodic banding seen along the axis of the fascicle as arising from (1) periodic arrangement of the orientation of the collagen fibers that make up the fascicle or (2) a period in the degree of the organization along the fiber axis [38]. It was determined by Diamant et al that the periodic pattern of light and dark bands, which depends on the angle between the axis of the actual segment of the fiber and the plane of polarization (Figure 14), correlated to the orientation of the collagen fibers along the tendon axis [38].

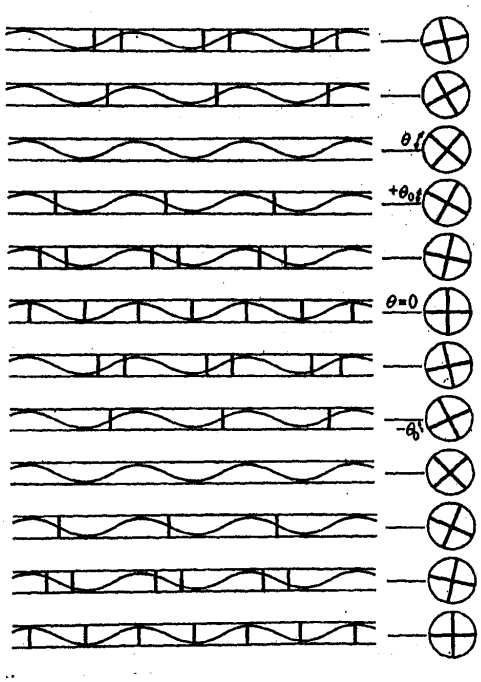

Figure 14 Diagram to explain the birefringence of collagen. The waves drawn within the tendons represent the periodically varying orientations of the collagen molecule across the full width of the tendon. The Polaroid directions corresponding to each rotation angle theta are to the right of the figure. Extinction occurs at those positions along the tendon where the tangent the wave coincides with one of the Polaroid directions. The extinction bands are the periodically spaced heavy lines that are perpendicular to the tendon. (Diamant, J, et al. (1972). *Ultrastructure of collagen as a function of ageing.* Proc R Soc Lond B, Vol 180, 293-315)

Collagen fiber crimp allows one to elucidate the structure-function relationship of collagen. An example of how collagen structure elucidates function is delineated below. In a previous study conducted in our lab, changes in collagen fiber crimp were measured and used to estimate local fiber strains. The collagen fiber crimp was measured in stress-free bovine pericardial tissue using a stereo optical microscope equipped with a CCD camera and trans-illuminated with polarized light. The tissue was then subjected to a 15% equibiaxial strain and fixed in glutaraldehyde to lock the collagen fiber crimp in place. The collagen fiber crimp was then measured again

following fixation in glutaraldehyde. It was found that after the application of 15% equibiaxial strain, the mean collagen fiber crimp period increased in value ranging 27 μm to 34 μm. On a specimen-by-specimen basis, this translated to an increase in fiber crimp period of ~15%, which is consistent with the externally applied strain level (Figure 15). This result indicated that, at least to a first approximation, the collagen fibers deformed similarly to the macro tissue strains. In other words, local fiber strains follow the external tissue strains. This result is consistent with a recent study by Waldman et al., in which it was determined that local fiber orientations were strictly dictated by the local tissue strains, and not by changes in specimen boundary loading conditions [40].

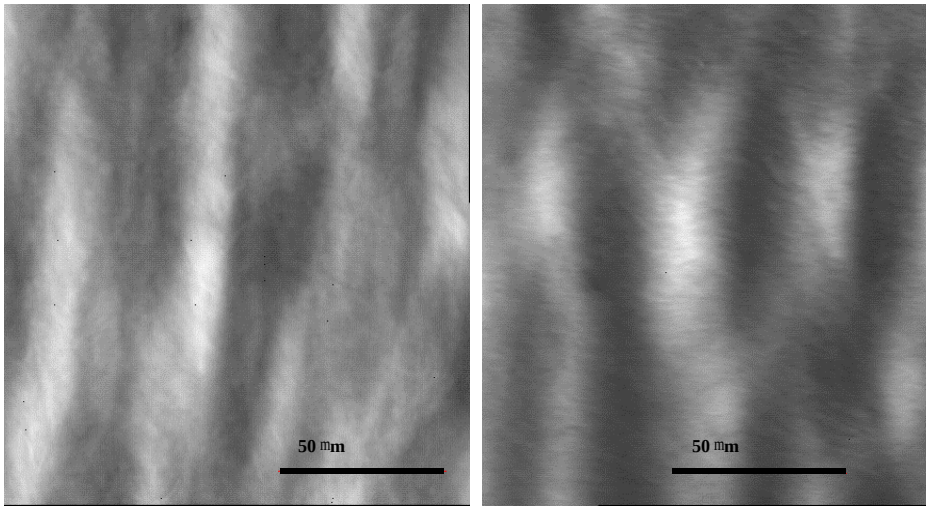

(a) (b)

Figure 15 Optical microscope images of native bovine pericardium showing the crimp at (a) reference and (b) 15% equibiaxial strain at approximately the same location in the tissue, demonstrating an increase in crimp period [41].

1.6.6 Evolution of Crimp

As for the evolution of crimp, there have not been many studies that have led to a firm conclusion regarding crimp formation. However, to date there exists two main possibilities for crimp initiation and development. One theory is based on a passive mechanical mechanism that is based on fiber buckling observed in fiber-matrix composites caused by shrinkage of the matrix [42]. Essentially a volume contraction of the proteoglycan versus the collagen component in the developmental stage occurs that induces bending of the collagen fibers. Another view is that crimp is initiated via cellular events involving active fibroblast participation. Fibroblasts have many contractile proteins and probably form some kind of junction when in contact. The ability of confluent growths of fibroblasts to actively contract collagen gels is well documented [43]. Because of this reason, the possibility of an active cellular role in crimp formation should be considered. In transmission electron microscopy sections, fibroblasts appear abundantly at crimp apexes, often in a bent form, as do the secreted collagen fibrils lying parallel to them. This is apparent when the cellular, rather than the fibrillar fraction are predominant [44]. However, more developmental observation must be made before any conclusions are made.

1.7 Composite Nature of Soft Tissues

Many soft tissues, including heart valve biomaterials such as bovine pericardial tissue, are biological composites of considerable complexity. While collagen type I is the main constituent of many components in the body, including tendons and the pericardial sac, pericardial tissue is not as regular oriented as the parallel-fibered tendon. The pericardial sac is a two dimensional meshwork with varying degrees of collagen orientation and constituent components (i.e. elastin) throughout the sac [45]. The degree of collagen orientation as well as the amount of elastin present in the tissue profoundly affects the mechanical behavior of the tissue. It has been shown previously in native and glutaraldehyde fixed calf pericardium that depending on where the tissue is removed from the pericardial sac, there is a marked non-homogeneity in the mechanical properties [45]. When selecting the pericardial tissue to be used for the BHV, care must be taken.

Heart valve biomaterials are structurally complex due to its composite-like composition and it is this attribute that helps to impart the excellent fatigue resistance. The excellent fatigue resistance is due mainly to the reinforcing phase of the composite while the lateral bonding between elements (fibers, microfibrils, etc) stabilizes the fibrous structure. The matrix, which consists of elastin, glycosaminoglycans, other proteins, water and mineral salts is the reinforced phase of the composite material. In any structure, the strength of the tension-bearing elements depends on the substance they are made of and their cross-sectional areas. Subdivision of a single element into multiple, parallel threads of equivalent cross sectional area like collagen fibrils has no effect on its ultimate strength while it yields two distinct side benefits [46]. According to the Cook-Gordon effect it is believed that by subdividing a single element into a network, the safety factor is increased. The Cook-Gordon effect states that an occasional crack is diverted and stopped at the surface of each wire, so it cannont propagate across a multi-thread rope as easily as it would cut through a single bar.

1.8 Background on Material Fatigue

Fatigue is the reduction of remaining strength or stiffness, and possible failure after a finite number of load cycles has been applied. Fatigue damage has been defined as the cycle dependent degradation of internal integrity, which is manifested in the loss of strength, loss of stiffness, and life of the material [47]. The safety, reliability, and durability of every engineering component rest directly on the understanding of the materials response to repeated cyclic loading or what is more commonly known as fatigue.

Traditional fatigue theories are applicable only to linear elastic rigid composites or other engineering materials, such as concrete or steel. These fatigue theories are not applicable because BHV undergo large deformations, have a non-linear stress strain curve, are highly anisotropic, and are structurally complex. To date, there are no existing theories that pertain to the fatigue of collagenous tissues nor are there acceptable theories for elastic composites.

The inherent anisotropy in heart valve biomaterials also further complicates fatigue phenomena [47]. The complex stress state associated with the fibers that may be aligned or arranged in some geometric fashion (i.e. strain aligned in preferred fiber direction) results in directional dependence of the mechanical properties of the tissue. This directional dependence can result in coupling between the fibers. Fiber coupling combined with complex internal stress redistribution are major influences in damage development [47]. The problem of stress redistribution is especially challenging when the synergistic effects of inhomogeneity and anisotropy are considered. As damage process alters the local geometry as a function of the number of applied cycles of loading, the internal stress redistributes continuously in time and gives rise to further damage development in a region or volume of material which becomes progressively

smaller. Ultimately this localization process creates a sufficiently intense local region of damage and stress that nucleates further until the entire heart valve fails [47].

Fatigue is a much more complex phenomena in collagenous tissues than in more familiar homogenous materials. Since collagenous tissue such as BHV are inhomogeneous, the numerous internal boundaries that separate constituent materials within the material can have different responses and different resistances to the long-term application of external influences. While the inhomogeneity of structure within a heart valve imparts its superior resistance to fatigue damage, inhomogeneity is also a significant contributing factor in initiation of damage at the micro level [47].

Understanding the mechanisms that lead to fatigue damage independent of calcification in a heart valve would allow one to control, quantitatively describe and predict the strength, stiffness, and life of a heart valve under long term loading in the presence of the fatigue effect. Further, with an understanding of the fatigue process, the estimated remaining life of a heart valve biomaterial would be able to be predicted.

1.9 Objectives and Aims of This Study

Current evaluation of BHV durability is performed using in-vitro accelerated wear testing. FDA guidelines require that the accelerated wear tester open and close the valve for a minimum of 200×10^6 cycles. One major limitation of this tester is that the flow field does not physiologically approximate in-vivo tissue stress fields. In addition to this limitation, accelerated wear testing is costly and time consuming. Another detriment is that the actual damage mechanisms are difficult to analyze due to the complexity of the BHV leaflet deformation during operation. Also, if an entire heart valve is used to elucidate how collagen structure is altered with repeated cyclic loading, the design of the heart valve (i.e. stent, stentless, etc), of which there would be many different designs to consider, would further confound interpretation of the materials'

response. Thus, the study of how collagen structure is altered with repeated loading must be independent of heart valve design.

The aim of this study is to gain an in depth understanding of the BHV biomaterials response to repeated cyclic loading, the mechanisms that reduce the strength, stiffness, and lifetime of the heart valve must be further explored. More specifically, to separate the effects of internal structural reorganization from actual fatigue damage in BHV biomaterial. The focus of this study is not to investigate the long-term fatigue properties of heart valve biomaterials but rather to elucidate the mechanisms that result in a loss of properties in heart valve tissue during the first $50x10^6$ cycles is to gain an in depth understanding of the underlying mechanisms of a collagenous tissue response to repeated cyclic loading.

To investigate the various underlying mechanisms, studies will be performed at two levels of hierarchy: tissue level, and the fiber level. At the tissue level, changes in collagen fiber network will be assessed and mechanical property changes will be quantified. In addition, the permanent set effects, which are changes in tissue geometry due to repeated cyclic loading, will be measured. At the fiber level, changes in collagen fiber crimp will be quantified and structural changes of the collagen triple helix will be qualitatively assessed using Fourier transform infrared spectroscopy (FT-IR).

Small angle light scattering will be used to assess the changes in collagen fiber architecture while multi-axial mechanical testing will be utilized to investigate mechanical behavior changes such as extensibility. Kinematical analysis based on deformation gradient derivations will be used to quantify changes in dimensions due to permanent set and it will also be utilized to help separate the effects of permanent set due to fatigue and actual changes in the collagen structure geometry. Collagen fiber crimp measurements will be taken pre- and post cycling to quantify changes in crimp. FT-IR spectral changes in the amide I carbonyl stretching region will be used to assess possible progressive collagen denaturation or loss of helicity.

2.0 METHODS

2.1 Small Angle Light Scattering (SALS) Presorting

A flowchart of methodologies used in this study is shown in Figure 16. Prior to any cycling, FT-IR analysis, or mechanical testing, SALS was used to presort the specimens. Following presorting, specimens were biaxial tested and FT-IR analysis was also performed. One specimen in each group was sacrificed for collagen fiber crimp measurements. After all of the baseline testing was performed, the specimens were mounted into the fatigue device and cycled to a level of $20x10^6$ and $50x10^6$ cycles. At each cycle stop level, all testing was repeated. At the $50x10^6$ level, in addition to FT-IR and biaxial testing, SALS testing was also performed.

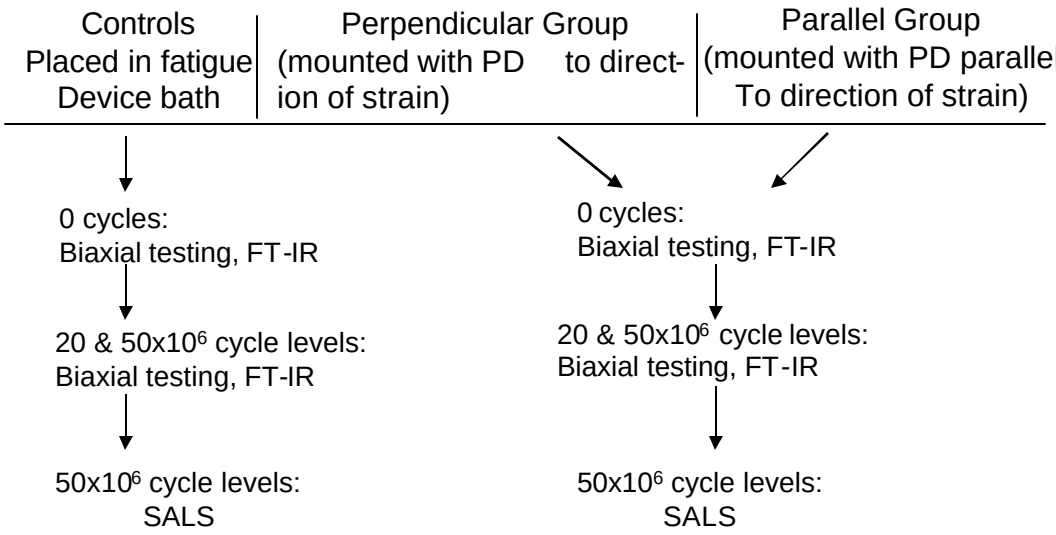

Figure 16 Flowchart of methodologies used in this study. Prior to any cycling, FT-IR, or mechanical testing, SALS was used to presort the specimens.

Because of the reported structural variability of bovine pericardium, a pre-selection protocol (pre-sorting) based on that developed for bovine pericardium [48] was utilized. A detailed description of the SALS device, analysis methods, and its accuracy in the tissue structural analysis previously has been presented [49]. Briefly, a 4 MW HeNe continuous unpolarized wave laser is passed through the tissue specimen, which scatters light according to the fiber structure within the light beam envelope. The resulting angular distribution of scattered light intensity about the laser axis, I(?), represents the distribution of the fiber angles within the light beam envelope at the current tissue location. The essential information obtained from I (?) distribution includes: (1) the preferred fiber direction, which is the centroid of I (?); and (2) an orientation index (OI), defined as the angle that contains 50% of the total number of fibers (Figure 17). *Note that highly oriented fiber networks will have low OI values while more randomly oriented networks will have larger value.*

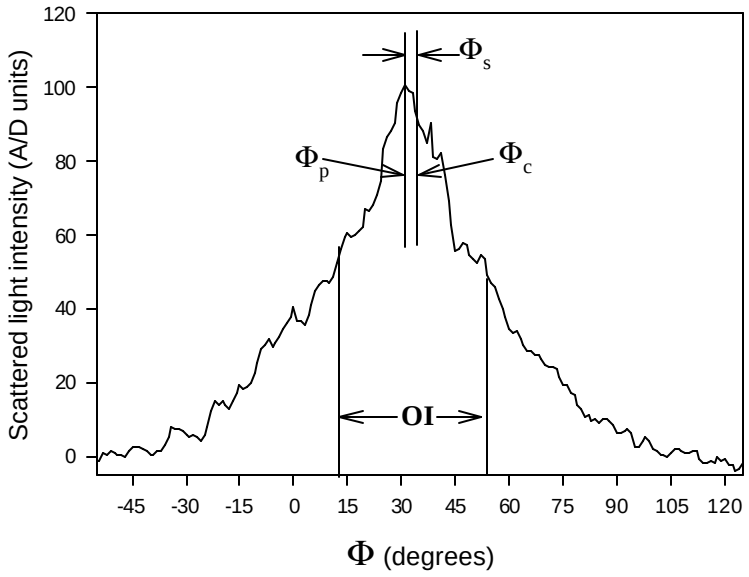

Figure 17 The I(Φ) vs. Φ data, showing the locations of Φ_p, Φ_c, and the definition of the distribution skew, $\Phi_s=\Phi_p - \Phi_c$.

The statistical distribution function of the angular distribution of the collagen fibers, $R(\theta)$, was also determined. $R(\theta)\,d\theta$ is defined as the fraction of collagen fibers oriented between θ and $\theta+d\theta$ and subjected to the normalization constraint $\int_{-\pi/2}^{\pi/2} R(\theta)d\theta = 1$. $R(\theta)$ was determined directly from the mean scattered light distribution $\bar{I}(\theta)$ for each specimen using

$$R(\theta) = \frac{\bar{I}(\theta)}{\sum_{\theta=-\pi/2}^{\theta=\pi/2} \bar{I}(\theta)\Delta\theta} \tag{1}$$

where, since $\bar{I}(\theta)$ is measured in discrete 1° increments [49], $\Delta\theta = \pi / 180$. For comparison to native heart valve fiber structure, the pericardial $R(\theta)$ demonstrated a broader distribution [50] (Figure 18).

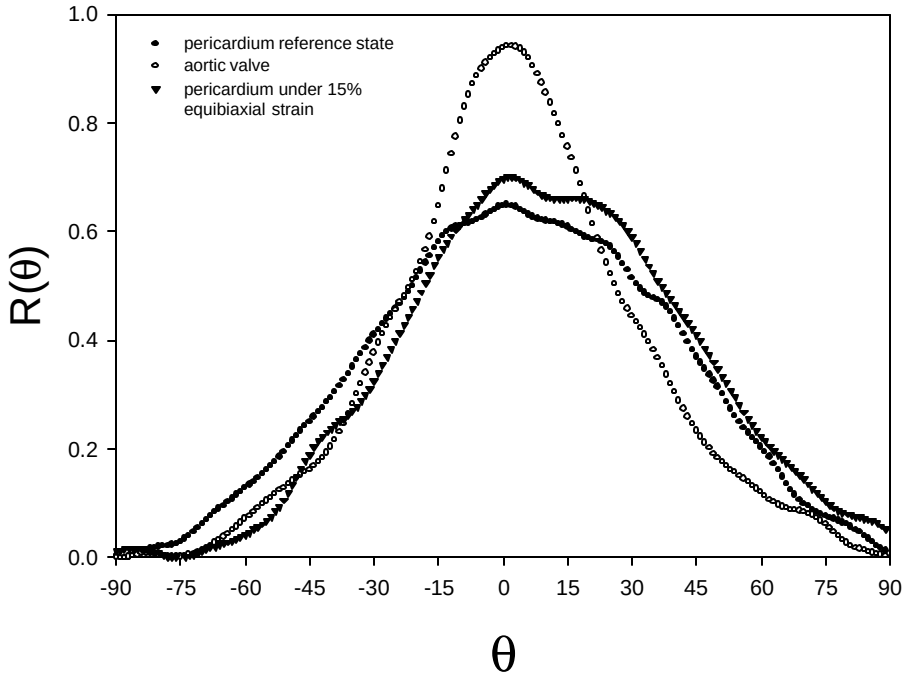

Figure 18 R(θ) for bovine pericardial tissue at the reference state (undeformed) and after 15% equibiaxial strain, demonstrating little change. Also shown is the R(θ) results for the aortic valve, which by comparison is a more highly aligned tissue[39].

Bovine pericardium was used in this study for two major reasons. Bovine pericardium is more structurally homogenous that aortic valve tissue and it is easier to work with because it comes in large 4 cm x 6 cm sheets. Bovine pericardium sheets were received and stored in a 0.625% glutaraldehyde solution at 4ºC. In order to make the bovine pericardium sheets fully transparent for small angle lights scattering (SALS) measurements, the sheets were cleared free floating in graded sugar solutions of 50, 75, and 87% for 1 h each. The pericardium sheets were stored in this solution until testing. Before performing the SALS tests, the bovine pericardium sheets, approximately 6 cm x 4 cm, were mounted flat in a thin vertical glass well free floating in the high sugar solution. SALS tests were then performed over the entire surface using a 2.54mm rectilinear sampling grid.

After SALS scanning, a customized program was used to identify 20 mm x 20 mm regions for biaxial testing. Selection was aided with a simultaneous display of the regional averaged preferred fiber directions and orientation index (OI). The SALS pre-sorting resulted in biaxial test specimens with a relatively high degree of structural uniformity. A total of 12 specimens and 6 controls were selected for fatigue testing. An example of a presorted specimen with the preferred fiber direction (PD) oriented along the X_1 biaxial testing apparatus axis and the cross preferred fiber direction oriented along the X_2 biaxial testing apparatus axis is shown in Figure 19.

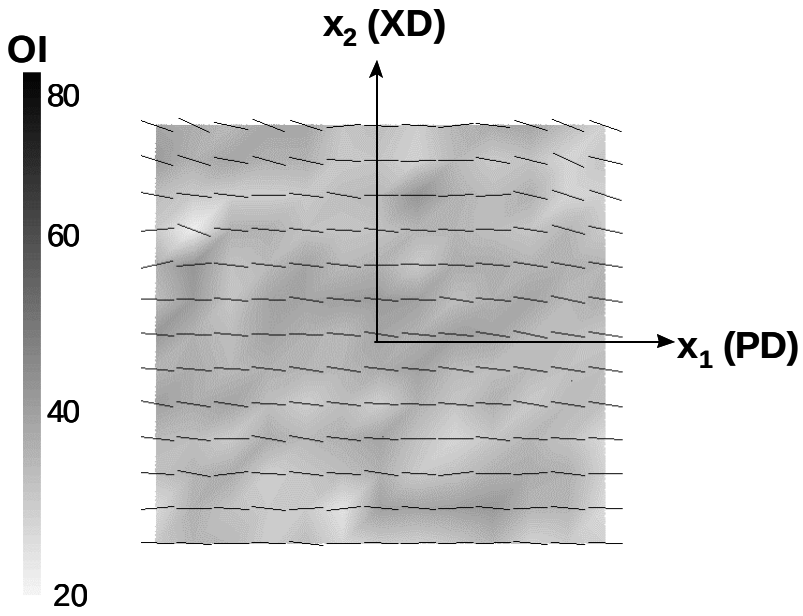

Figure 19 Presorted biaxial specimen with the PD oriented along the X_1 axis and the XD oriented along the X_2 test axis. Lines indicated the orientation of the fibers. Darker regions correspond to more highly aligned areas whereas lighter regions correspond to areas with a lesser degree of orientation.

SALS structural presorting was confirmed using biaxial testing methods previously reported [51]. The four specimen marker positions, used for biaxial testing, were recorded prior to mounting the specimens into the fatigue device to quantify the mechanical effects of fatigue.

2.2 Fatigue Testing

2.2.1 Device Design Criteria

The testing system used in this study applied a dynamic uni-directional tensile load. Tensile loading was chosen for two reasons. An upper limit tissue response was desired so tensile loading was utilized. Tensile loading is the most extreme loading case because it induces exaggerated fiber rotations. It was thought that the greated changes in the tissue would occur with tensile loading. In addition to this reason, it has been documented in conversations with a collaborator in industry that that the primary structural failure mode in bovine pericardial valves is tensile induced tears (Personal communication with Michael Scott, P.h.D. of Edwards Life Sciences).

A maximum cycle level of $50x10^6$ cycles was chosen for two reasons. In a previous fatigue study in our laboratory, the stability of the chemically treated porcine BHV collagen fiber architecture during long-term valve operation was investigated [52]. The glutaraldehyde treated porcine BHV were subjected to 0, $1x10^6$, $50x10^6$, and $200x10^6$ in vitro accelerated test cycles. It was found that the native collagen architecture of the porcine BHV was rapidly and irreversibly lost after only $50x10^6$. The focus of this study is on the initial fatigue responses to cyclic loading with the premise that any chemical modification to tissue that can be developed to improve durability of the tissue would have to act in this initial period. Once the fatigue process has set in, there is not much that can be done in terms of prevention. In addition to this, in advanced fatigue conditions, the tissue becomes very difficult to work with because of the damage to the

tissue. Thus, in the present study, GLBP was subjected medium-term tensile only cyclic loading.

A commercially available biomedical cyclic loading device (ELF 3200, EnduraTEC, Minnetonka, MN) was modified in such a way that it could hold an apparatus designed for such specific testing purposes (Figure 21 a & b). The device holds 12 specimens and the specimens were all loaded equally by utilizing a system that monitored and recorded individual load data without user intervention. The effects of long-term cyclic creep were considered and a mechanism was devised to adjust specimen length along the direction of loading which would enable the user to maintain the desired load over time. The experiment was conducted at room temperature and a filtering system was attached to the bath.

2.2.2 Principle of Device Operation

The apparatus (Figures 20 a & b), built by Daniel Hildebrand of the Engineered Tissue Mechanics Laboratory, was designed to allow for the application of a dynamic, uniform uni-directional stretch to twelve rectangular soft tissue specimens [53]. The specimens are mounted to two arms, one stationary and one moveable (Figure 21). The moveable arm is displaced vertically via its connection to the cyclic loading device (ELF 3200, EnduraTEC, Minnetonka, MN). The specimens were stretched based on the displacement of the actuator of the cyclic loading device. In order to compensate for long-term creep effects, tension in the specimens was controlled by turning a thumbscrew which strains the individual specimen to varying degrees during the cycling. The fixtures can were adjusted vertically and horizontally with respect to the specimen in order to maintain on axis loading. Load measurements were monitored with load cells (SML-25, Interface, Scottsdale, AZ) mounted inline with each specimen and attached to the stationary arm. Load data was read and stored at user definable rate to a PC for post testing analysis. Continuous visual inspection of the specimens was permitted because of the translucent polycarbonate viewing panels. Both the stationary and moveable assemblies are contained within a water tight, triangularly shaped, bath

enclosure. Specimens were loaded outside of the bath environment and the sterility was maintained via the bath's connection to a variable temperature liquid pump (Supertemp 200D, PolyScience Corp, Niles, IL) and a 0.2 micron rated membrane filter (McMaster-Carr Company, Cleveland, OH). Specimen grips consisted of a T-slotted mount on which rides two short rectangular pieces with four small diameter holes drilled in a linear pattern. A 316L stainless steel wire pin was fitted through each of the holes. In this way, when the two parts are brought together with the specimen in between the grips, the specimen is clamped firmly in place. The pin pattern duplicates the holes used for biaxial mechanical testing.

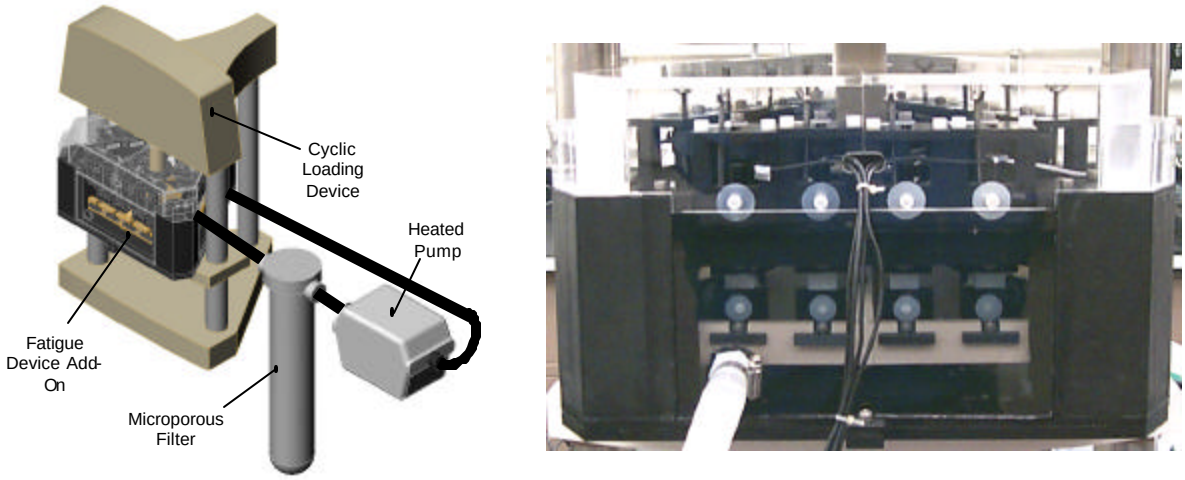

(a) (b)

Figure 20 Computer modeled representation of the testing apparatus in place with commercial cyclic loading device (a) and a picture of the fatigue device add-on while not operating (b).

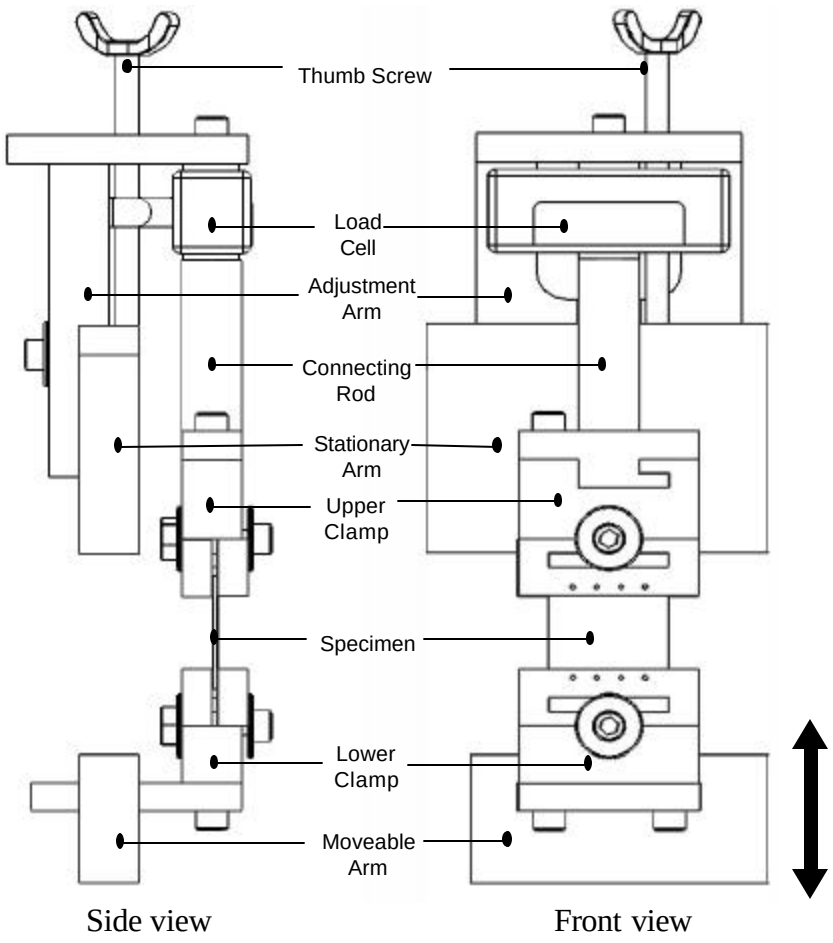

Figure 21 Schematic of device operation. Specimen is mounted between grips with pins inserted in biaxial testing locations. Specimen is stretched by displacement of lower moveable arm. Individual specimen strain can be adjusted by turning the thumbscrew.

2.2.3 Design: Electronic Control

Each of the twelve load cells (temperature compensated, 25 lb. load capacity, 0.05% error; model # SML-25, Interface, Scottsdale, AZ) were connected to an integrated signal conditioner and amplifier (500-2-10, Interface Electronics, Scottsdale, AZ) via shielded 22 gauge, stranded cable to reduce signal interference. The amplifiers were powered by a 24V DC power supply (SOLA, Skokie, IL). The signal conditioner/amplifier and power supply were housed in a polycarbonate container. Load cells were calibrated by first zeroing the output voltage, then applying a 1 kg load and adjusting the output voltage until it meets the calculated output voltage using the

factory measured mV/V calibration factor. The linearity of the calibration in the range of testing was verified using 0.50 kg and 0.20 kg weights. Peak load data were acquired with software written in Labview and stored on the computer. Real-time monitoring of individual loads was done with the software to ensure a proper sinusoidal load waveform (Figure 22).

The bath solution was a phosphate buffered saline solution kept at room temperature (25° C). Six fatigue specimens were mounted into the tester with the direction of strain aligned in the tissue PD [49] while the cross-preferred fiber direction (XD) was not loaded (Figure 23 b). Six additional specimens were loaded

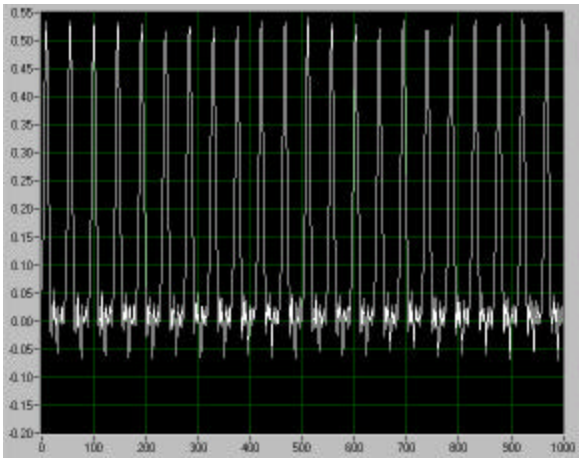

Figure 22 Representative load (kg-f) at 22 Hz loading rate plotted against number of specimens acquired. The total number of specimens in this plot corresponds to 1 second (1 kHz sampling rate).

with the XD direction perpendicular to the direction of strain (Figure 23 a). Six control specimens were put into the same testing bath, without any loading imposed on, for characterizing the time and solution effects.

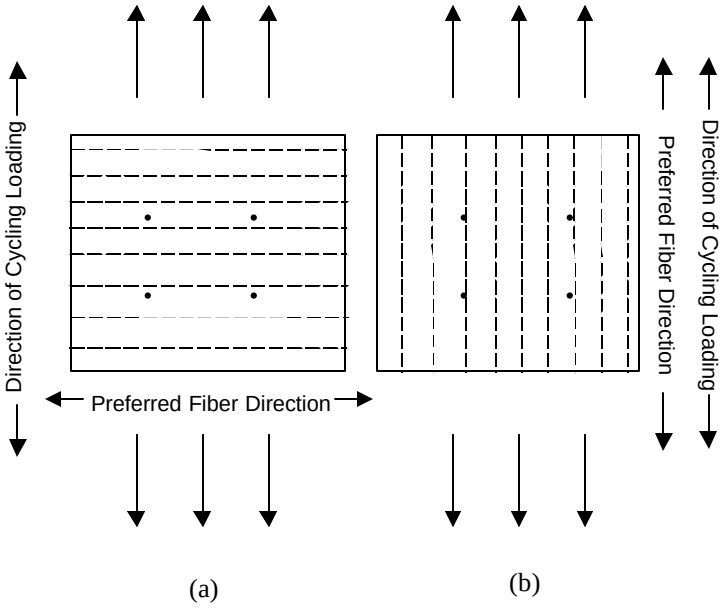

Figure 23 – Schematic showing the specimen with the preferred fiber direction (PD) mounted perpendicular to the cyclic load (a) and with the preferred fiber direction parallel to the cyclic load (b).

The specimens were subjected to a stress level of 500±50 kPa at a frequency of 22 Hz. The stress level was determined on an individual specimen basis by adjusting the displacement levels of the specimens with the thumbscrews. Care was taken to make sure the specimens did not buckle with the given displacement levels. Over time, cyclic creep effects necessitated that the load be periodically increased by stretching the specimens with the thumbscrews. A stress level of 500±50 kPa was chosen because finite element simulations estimated valves stresses to be ~250-300 kPa [54, 55]. Some areas of the valve may experience greater stresses (i.e. attachment to stent, commisure regions) so the stress level was approximately doubled to compensate for this. A frequency of 22 Hz was chosen because loading and unloading time of the valve corresponds to approximately 20 Hz.

2.3 Biaxial Mechanical Testing

Prior to mounting the specimens into the fatigue device for cycling, the specimens were biaxial tested. The biaxial testing device and methods have previously been described in detail elsewhere [51]. In general, biaxial testing of biological tissues are performed using thin specimens, which are either a membrane in its native form or a thin section prepared from a thick tissue slab. The specimen is mounted to the biaxial device in trampoline-like fashion using thin threads, which allows the edges to expand freely in the lateral direction (Figure 24a). Testing is generally performed with the specimen completely immersed in phosphate buffered normal saline (pH 7.4) at room temperature. The central target region must be sufficiently small and located away from the outer edges to avoid the tethering effects. Thus, in the central target region the stress and strain field is generally considered homogeneous, so that the components of **F** are independent of position.

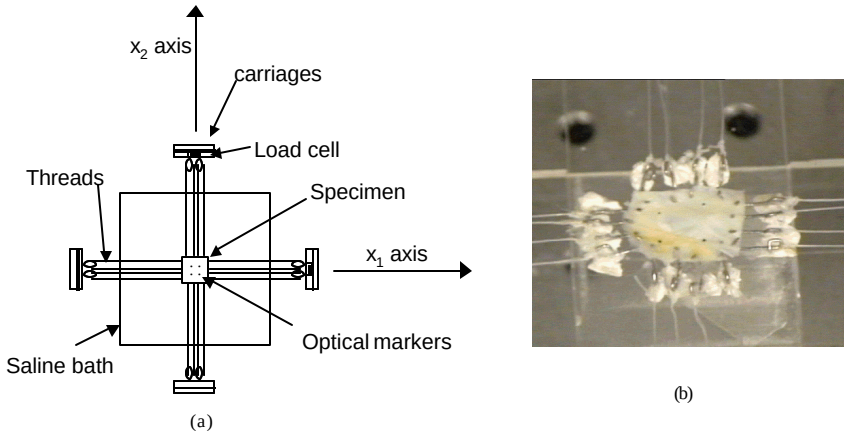

Figure 24 (a) Schematic of the biaxial testing setup. (b) Photo of a specimen at 1MPa peak equi-biaxial stretch.

A Lagrangian stress controlled test protocol was utilized, where Lagrangian stress (**T**) is defined as the force per unit of original area. A stress-control protocol was utilized because stress controlled biaxial tests allow for a wider range of stress and strain, especially in generating a negative strain state that are difficult to reproduce in a strain-controlled test. Also, physiologically native and BHV tissues are loaded by transvalvular pressure, which is similar to a stress-control test.

Tissue specimens were first preconditioned with 10 cycles of equi-biaxial stretch (T_{11}:T_{22} = 1.0:1.0). To capture fully the response over the functional range, a maximum stress level of 1MPa was used, which is estimated to be four times the nominal stresses of 250 kPa in the BHV [54] [55] (Figure 24b). Preconditioning was followed by the following T_{11}:T_{22} ratio controlled protocols were run: 1.0:0.75, 0.75:1.0, 1.0:0.5, 0.5:1.0, 1.0:0.30, 0.30:1.0, 1.0:0.2, 0.2:1.0, 1.0:0.1, 0.1:1.0 and 1.0:1.0. Equi-biaxial tests were also performed before and after testing to verify the stability of the mechanical response.

2.3.1 Post Fatigue Biaxial Testing

After $20x10^6$ and $50x10^6$ cycles, the specimens were removed from the fatigue device and recovered for 24 hours in phosphate buffered saline solution at 4 C. After $20x10^6$ cycles, some of the specimens holes where the pins had been inserted, which are also where the sutures are inserted during biaxial testing, were enlarged. Some of the enlarged holes were large enough so the biaxial test sutures would fall out during biaxial testing. These specimens were trimmed where the holes were made and new holes were made for the sutures.

The camera of the biaxial testing device was calibrated before commencement of biaxial testing to ensure a comparable strain measurement to the level. It is essential that the camera was calibrated correctly because the positions of the graphite optical markers in the unloaded state at $0x10^6$ cycles were used to quantify the effects of cycling. Some graphite optical markers did fall off during handling and testing but care was taken to make sure that the markers were returned in the same location, which was often easy to locate due to the residue of the glue used to attach the graphite markers.

The biaxial testing of all specimens was completed within four days after the specimens were removed from the fatigue tester. The same biaxial testing protocol for the specimens at the $0x10^6$ cycle level was utilized for both the controls and specimens.

2.3.2 Kinematics of Biaxial Testing

The first step in defining large deformation gradient tensor strain measures is to define the relationship between what is known as the reference, initial or undeformed configuration of a body, and the deformed configuration of the body. The reference or undeformed configuration is the condition of a body in space before loads have been applied to it. The deformed configuration is the location and shape of the body after the loads have been applied to it. Under biaxial loading, the following *homogeneous* (i.e. independent of position) biaxial deformation is represented as

$$x_1 = \lambda_1 X_1 + \kappa_1 X_2, \; x_2 = \lambda_2 X_2 + \kappa_2 X_1, \; x_3 = \lambda_3 X_3 \tag{1}$$

where $\mathbf{x}$ and $\mathbf{X}$ the position vectors representing the locations of material particles in the reference and deformed states, and λ_i are the axial stretch ratios and κ_i measures of in-plane shear. The deformation gradient tensor $\mathbf{F}$ maps the reference state to the deformed state. λ_i and κ_i are also components of the deformation gradient tensor $\mathbf{F}$, which for deformation described in eqn. 1 is

$$\mathbf{F} = \begin{bmatrix} \frac{\partial x_1}{\partial X_1} & \frac{\partial x_1}{\partial X_2} & \frac{\partial x_1}{\partial X_3} \\ \frac{\partial x_2}{\partial X_1} & \frac{\partial x_2}{\partial X_2} & \frac{\partial x_2}{\partial X_3} \\ \frac{\partial x_3}{\partial X_1} & \frac{\partial x_3}{\partial X_2} & \frac{\partial x_3}{\partial X_3} \end{bmatrix} = \begin{bmatrix} \lambda_1 & \kappa_1 & 0 \\ \kappa_2 & \lambda_2 & 0 \\ 0 & 0 & \lambda_3 \end{bmatrix} \tag{2}$$

$\mathbf{F}$ is a critical mathematical quantity since it completely describes the deformation state. However, $\mathbf{F}$ cannot be used to directly for strain characterization because it contains rigid body motions. Since soft tissues are composed primarily of water and have negligible permeability [24], they can be considered incompressible so that $J=\det\mathbf{F}=1$. From $\mathbf{F}$ the components of the in-plane Green-Lagrange strain tensor is defined as $\mathbf{E} = ½$

($\mathbf{F}^T\cdot\mathbf{F} - \mathbf{I}$), where $\mathbf{I}$ is the identity tensor. $\mathbf{E}$ is a mapping that quantifies the deformed length changes when going from the initial configuration to the deformed configuration. It is independent of rigid body motion. In practice the components of $\mathbf{E}$ are computed more directly using:

$$E_{11}=\frac{1}{2}\left(\lambda_1^2+\kappa_2^2-1\right),\quad E_{12}=\frac{1}{2}\left(\lambda_1\kappa_1+\lambda_2\kappa_2\right),\quad E_{22}=\frac{1}{2}\left(\lambda_2^2+\kappa_1^2-1\right) \tag{3}$$

$\mathbf{E}$ is the most common finite strain measure in the soft tissue literature due to the simplicity of the constitutive formulations.

As mentioned above, the components of $\mathbf{F}$ are determined optically to avoid any mechanical interference with the specimen. This is typically done by tracking the position of markers mounted on the upper specimen surface that delimit the central target region using optical tracking software [48] [56]. Because $\mathbf{F}$ is based on a continuous function and the marker positions are discrete functions, interpolation is needed to transform the Cartesian (discrete marker positions) coordinates to natural coordinates, which is a continuous function. In both our laboratory [48] and in others [57, 58], finite element shape functions are used to approximate the position vector field within the central target regions. This can include linear and quadratic variations in strain [50]. In both our laboratory [48] and in others [57, 58], finite element shape functions are used to approximate the position vector field within the central target regions. Thus, the displacement field $\mathbf{u}$ (=$\mathbf{x}$-$\mathbf{X}$) at any time or location within central target region can be determined using

$$\mathbf{u}(r,s)=\sum_{n=1}^{m} f_n(r,s)\,\mathbf{u}_n \tag{5}$$

where f_n are the shape function of node (or equivalently marker) n, m is the total number of nodes (markers), and r,s are the isoparametric coordinates [59] where the displacement is to be determined (Figure 25). Since eqn. 5 represents a linear sum of m equations where only f_n are functions of r,s, the spatial derivatives of u_i with respect to r,s are given by

$$\frac{\partial \mathbf{u}}{\partial r} = \sum_{n=1}^{m} \frac{\partial f_n}{\partial r}\,\mathbf{u}_n \qquad \frac{\partial \mathbf{u}}{\partial s} = \sum_{n=1}^{m} \frac{\partial f_n}{\partial s}\,\mathbf{u}_n \tag{6}$$

The spatial derivatives with respect to **x** are determined for u_1 and u_2 by substitution into the following relations and inverting [60]

$$\begin{bmatrix} \dfrac{\partial}{\partial r} \\ \dfrac{\partial}{\partial s} \end{bmatrix} = \begin{bmatrix} \dfrac{\partial u_1}{\partial r} & \dfrac{\partial u_2}{\partial r} \\ \dfrac{\partial u_1}{\partial s} & \dfrac{\partial u_2}{\partial s} \end{bmatrix} \begin{bmatrix} \dfrac{\partial}{\partial x_1} \\ \dfrac{\partial}{\partial x_2} \end{bmatrix} \tag{7}$$

The components of **F** at each time point can be determined using

$$\mathbf{F} = \mathbf{H} + \mathbf{I} = \begin{bmatrix} \dfrac{\partial u_1}{\partial X_1} & \dfrac{\partial u_1}{\partial X_2} \\ \dfrac{\partial u_2}{\partial X_1} & \dfrac{\partial u_2}{\partial X_2} \end{bmatrix} + \begin{bmatrix} 1 & 0 \\ 0 & 1 \end{bmatrix} = \begin{bmatrix} \lambda_1 & \kappa_1 \\ \kappa_2 & \lambda_2 \end{bmatrix} \tag{8}$$

where $\mathbf{H} = \partial\mathbf{u}/\partial\mathbf{X}$.

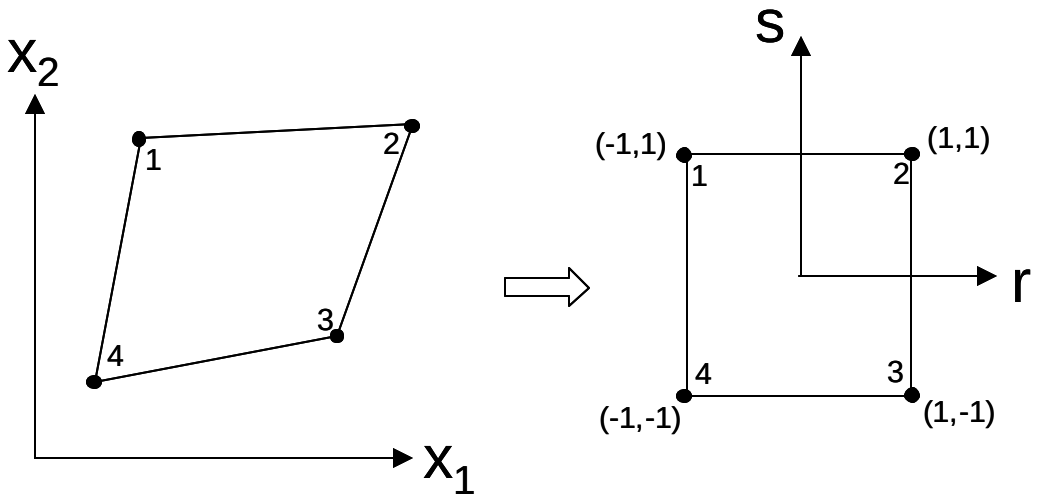

Figure 25. Mapping of the real-time positions of four tissue markers from the original device coordinates (x_1,x_2) to the isoparametric coordinates (r,s), allowing for bi-linear interpolation of the displacement field.

Areal stretch is defined as the overall tissue compliance. It is a measure of the overall area changes within the strain tracking markers. Areal stretch is computed using the following equation:

$$\text{Areal stretch} = [(\lambda_1 * \lambda_2 - \kappa_1 * \kappa_2) - 1] * 100\ \% \qquad (9)$$

where λ_1 is the peak axial stretch in the PD while λ_2 is the peak axial stretch in the XPD.

2.3.3 Forces and Stress

As mentioned above, biaxial testing of biological tissues was performed using thin specimens (no more than ~3 mm, usually <1 mm) and acted on by only in-plane loads. A state of plane stress is thus assumed so that the components t_{i3} (i=1,2,3) of the Cauchy stress **t** (force / deformed area) are 0. Practically, during actual experiments one can measure the initial specimen dimensions, so that the Lagrangian stresses **T** (force / unit original cross-sectional area) are used for convenience. The components of **T** are computed from the measured axial forces **P** using

$$T_{11} = \frac{P_1}{hL_2}, \quad T_{22} = \frac{P_2}{hL_1} \qquad (10)$$

where H the specimen thickness and L_i the specimen lengths (Figure 26). The Lagrangian stress gives us the actual force rendered in the undeformed surface area. Since experimentally applied loads are normal to the edges, $T_{12}=T_{21}=0$. The 2nd Piola-Kirchhoff stress tensor **S** is the most commonly utilized stress tensor for soft tissue constitutive theories, and is determined using $\mathbf{S=T\ F^{-1}}$. The Cauchy stress tensor **t** is determined using $\mathbf{t=F\ T}/J$, which in component form are given by (with $T_{12}=T_{21}=0$):

$$t_{11} = \lambda_1 T_{11},\ t_{22} = \lambda_2 T_{22},\ t_{12} = \kappa_1 T_{22},\ t_{21} = \kappa_2 T_{11} \qquad (11)$$

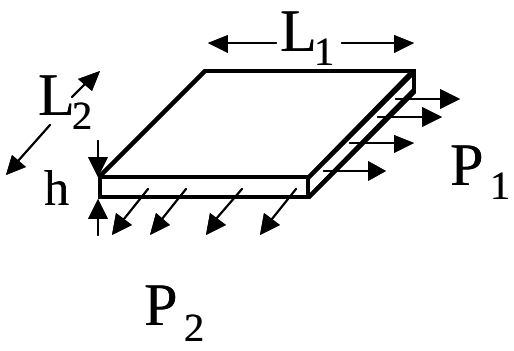

Figure 26 Schematic of a biaxial specimen

In the case where there is negligible shear strain (i.e. E_{12}~0), the normal components of the two stress tensors are related by:

$$S_{11} = T_{11}/\lambda_1,\ S_{22} = T_{22}/\lambda_2 \qquad (12)$$

2.3.4 Kinematic Analysis

To quantify mechanical property changes during cyclic loading, the biaxial mechanical testing data was analyzed with respect to both (i) the current reference marker positions, and (ii) the original un-cycled reference marker positions. This approach allows examinations of current tissue mechanical properties with respect to both the permanent deformation (permanent set) caused by the cyclic loading and the loading deformation due to the application of 1 MPa in biaxial testing. To rigorously quantify multi-dimensional tissue deformation during fatigue, we rely on the kinematic framework of finite strain theory with multi-configurations. These relations can be explained as follows. Consider the relations between the three configurations of interest: the initial, stress-free uncycled configuration $ß_0^0$, the stress-free but fatigued configuration $ß_1^{n\ cycles}$, and the loaded configuration $ß_2^{n\ cycles}$ for the state when the tissue is stressed to 1 MPa (Figure 27). The deformation gradient tensor **F** associated with the any

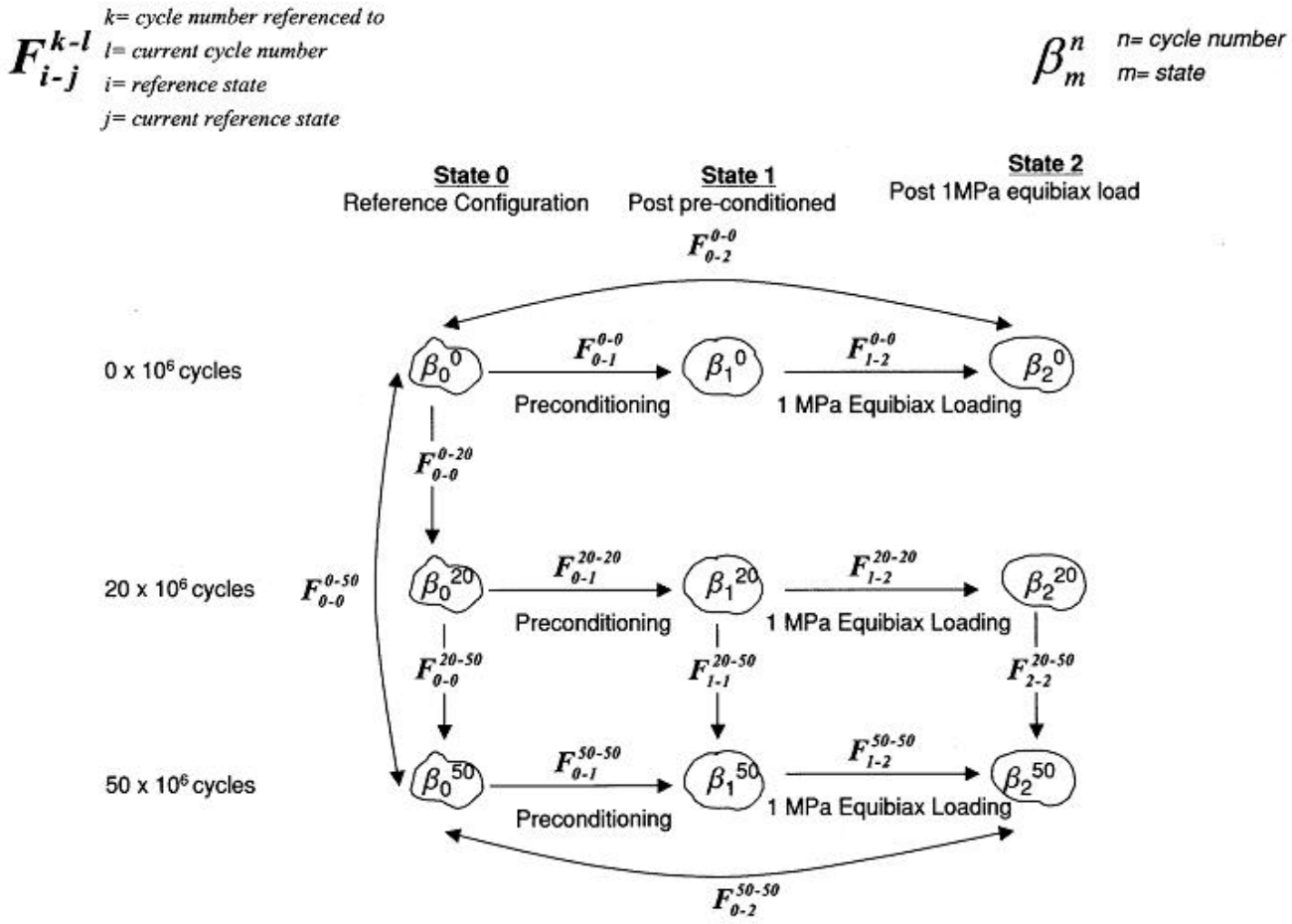

Figure 27 Deformation gradient derivations.

finite deformation is given by $\mathbf{F}_{\text{2-Dim}} = \begin{bmatrix} \lambda_1 & \kappa_1 \\ \kappa_2 & \lambda_2 \end{bmatrix}$, where λ_i are the stretch ratios and κ_i measures of in-plane shear. When deforming from $ß_0^0$ to $ß_1^0$, $ß_1^0$ to $ß_2^0$, $ß_0^0$ to $ß_2^0$ (Fig. 32), the associated deformation gradient tensors are F_{0-1}^{0-0}, F_{1-2}^{0-0}, F_{0-2}^{0-0} respectively. Extending this approach to the current study, we adopt the notation F^{0-0}, F^{20-20}, and F^{50-50} for the 1 MPa equibiaxial loading induced deformations at 0, 20 and 50x10^6 cycles, respectively. Thus, F_{1-2}^{20-20} and F_{1-2}^{50-50} represent the deformations due the application of 1 MPa equibiaxial loading analyzed with respect to the current reference

marker position. In contrast, $F_{0\text{-}2}^{0\text{-}20} = F_{0\text{-}0}^{0\text{-}20} F_{0\text{-}2}^{20\text{-}20}$ and $F_{0\text{-}0}^{0\text{-}50} = F_{0\text{-}0}^{0\text{-}50} F_{0\text{-}2}^{50\text{-}50}$ represent the data analyzed by referenced to the initial, un-cycled reference marker position. In the present study, when mechanical testing data is referred to the initial, stress-free uncycled configuration $ß_0^0$ and no changes are observed, it can be concluded that there are no intrinsic changes in the mechanical properties of the tissue, and that the observed changes in the current state represent "permanent set" effects only.

The stretch ratios along the preferred ($_{PD}$) and cross-preferred ($_{XD}$) directions under 1 MPa equibiaxial stress was used to quantify the tissue extensibility. The net tissue compliance was represented by the areal stretch that was computed (= $_{PD}$ $_{XD}$) under 1 MPa equibiaxial stress. Comparisons between cyclic loading levels were performed using t-tests, with statistically significant difference level set to $p<0.05$. All data are represented as the mean standard error.

2.4 Collagen Crimp

2.4.1 Histology Preparation for Crimp Analysis.

At $0x10^6$ and $50 x10^6$ level, two specimens were sacrificed in both the preferred and cross-preferred fiber direction (Figure 28). At $20x10^6$ cycles level, one specimen was sacrificed in the preferred and cross-preferred direction for histology. En face sections were prepared from two millimeter wide specimens that had the preferred fiber direction parallel to the cut were prepared as indicated in figure. The histological specimens were stained for Pico Sirius red, which makes the collagen birefringent when viewed under polarized light, and permanently prepared under a coverslip. Subsequent polarized light microscopy (Nikon Eclipse Microscope) was performed on each specimen and numerous digitized images were recorded (n=3-6). At each

magnification (e.g. 10x, 20x, and 40x), a stage micrometer was digitally imaged and recorded for subsequent validation of the collagen fiber crimp.

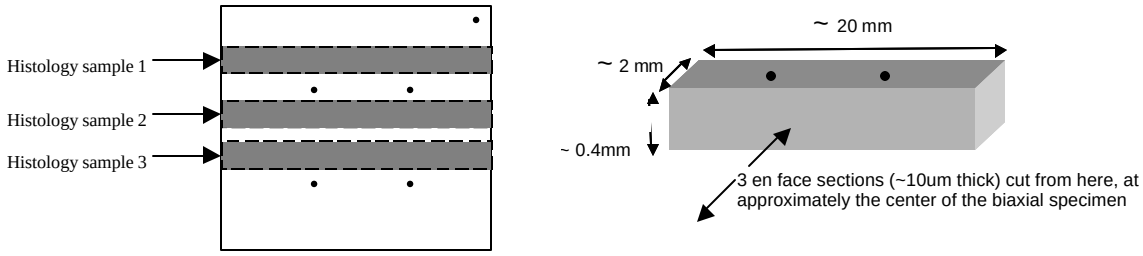

Figure 28 Histology selection. Specimens were cut parallel to the direction of PD away from the edges so as to avoid the suture holes

2.4.2 Calculation of Collagen Fiber Crimp

In order to enhance the natural birefringence of collagen, picro Sirius red stain is used. Collagen molecules are rich in basic amino acids so therefore they react strongly with acidic dyes. Picro Sirius Red, a strongly acidic dye, reacts with collagen and promotes an enhancement of its normal birefringence. This enhancement of birefringence using Picro Sirius Red and polarization is a common method used to study the crimp patterns of collagen [61].

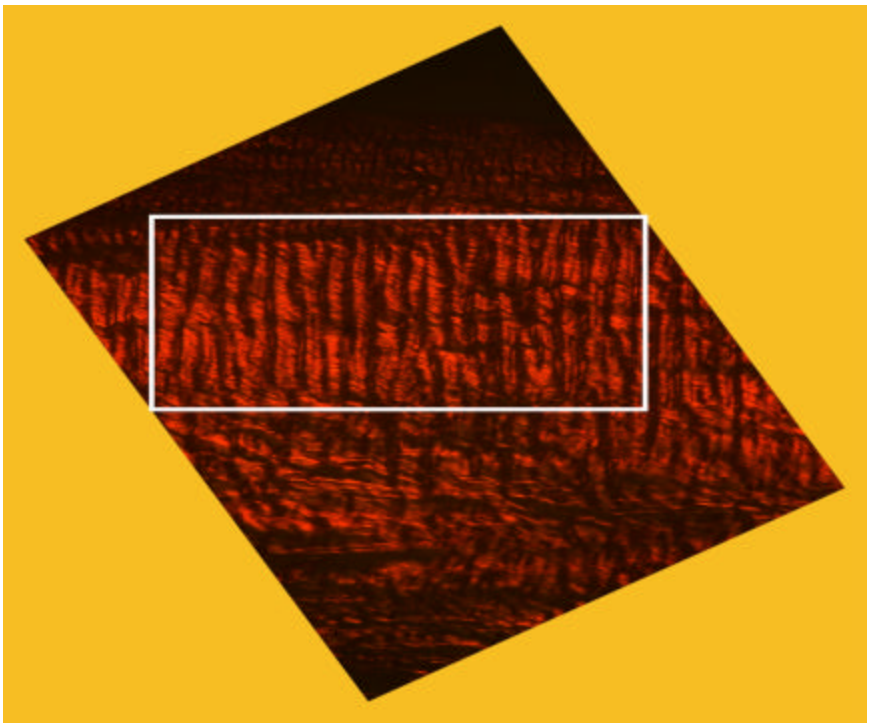

Figure 29 Polarized digital photomicrograph (20x magnification) from the mid-belly region of a zero-pressure fixed porcine bioprosthetic heart valve (PBHV) after accelerated cyclic loading up to 200×10^6 cycles. The rectangle signifies the N (rows) by M (columns) image matrix of pixel intensities for importation into MATLAB® for analysis of the collagen fiber crimp period.

Digital polarized photomicrographs (Figure 29) taken of the bovine pericardium were imported as N (rows) by M (columns) matrices of grayscale pixel intensities into MATLAB® (TheMathWorks, Inc., Ver. 7.0). The images were then averaged along the columns; creating a vector of averaged intensities having the dimension of 1 (row) by M (columns). This vector was next entered as a *discrete intensity versus distance signal* (Figure 30) into the MATLAB Signal Processing Toolbox®, where a fast Fourier transform (FFT) and power spectral density (PSD) were subsequently performed (Figure 31).

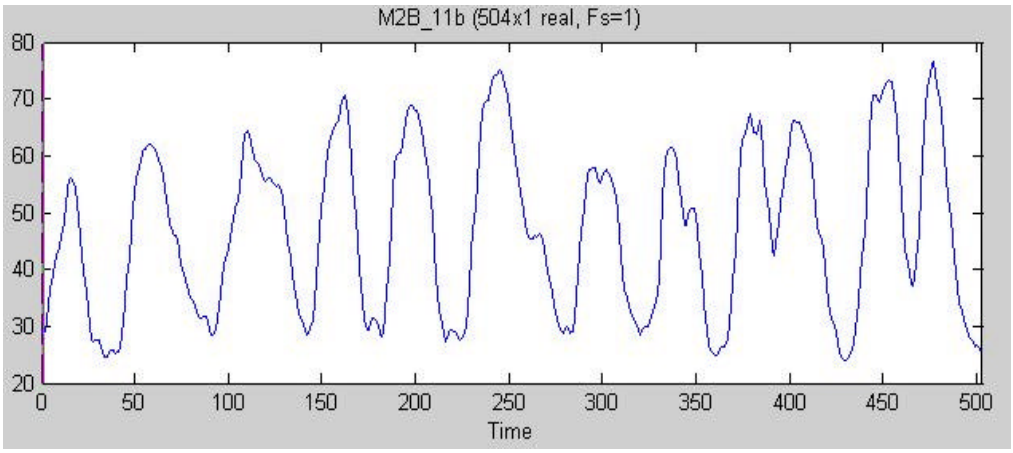

Figure 30 Signal plot of the column-averaged pixel intensities for the image matrix outlined in Figure 30. They x-axis represents the width of the matrix in pixels, while the y-axis is an arbitrary intensity scale. One can roughly estimate the crimp period (?) at 45 pixels. However, fast Fourier transform (FFT) and subsequent power spectral density (PSD) analysis is required to accurately calculate the overall crimp period.

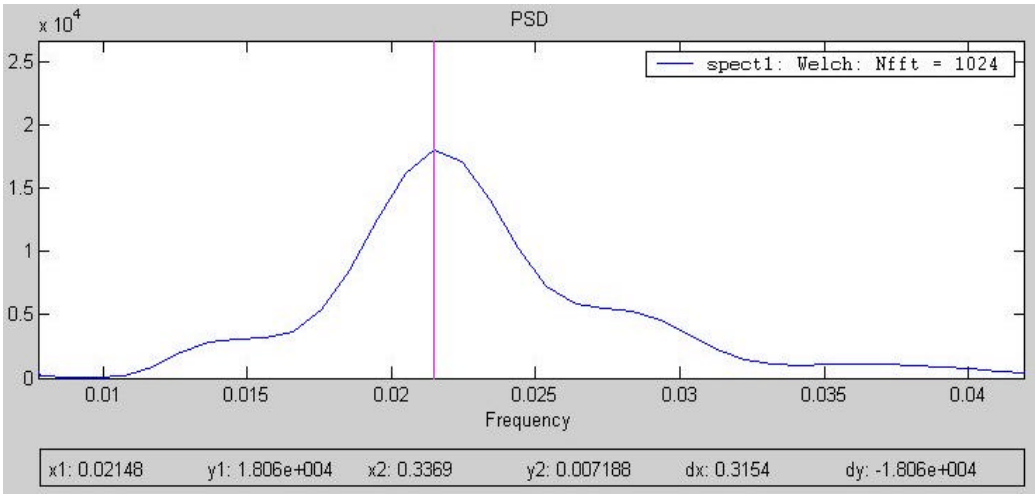

Figure 31 Spectral decomposition (PSD) results in a defined peak centered about 0.02148 Hz (pixels^{-1}). On inversion, this corresponds to a crimp period of 46.55 pixels. This calculated period is in dose agreement with the rough estimation in Figure 31. Using the conversion factor of 1.5 pixels / micron, derived from a calibrated stage-micometer (also at 20x magnification), we arrive at the final collagen fiber crimp measurement of 31.03 microns for this particular photomicrograph.

A signal can be viewed from two different domains: (1) the time domain and (2) the frequency domain. The most common one is the time domain. This is the trace on an oscilloscope where the vertical deflection is the signals amplitude, and the horizontal deflection is the time variable. The second representation is the frequency domain. This is the trace on a spectrum analyzer, where the horizontal deflection is the frequency variable and the vertical deflection is the signals amplitude at that frequency. Any given signal can be fully described in either of these domains. One can go between the two by using a tool called the *Fourier Transform.* Depending on what is done with the signal, one domain tends to be simpler than the other, so rather than getting tied up in mathematics with a time domain signal a frequency domain is used because the math is a lot simpler.

The *Fourier transform*, in essence, decomposes or separates a waveform or function into sinusoids of different frequency which sum to the original waveform. It identifies or distinguishes the different frequency sinusoids and their respective amplitudes [62]. Although Hilbert et al. have previously reported successful calculation of collagen crimp periods using similar optical methods [63], investigators have not continued such digital image analysis beyond FFT [64]. The use of PSD after FFT of the intensity signal accounts for variations in the quality of a digital image that may be mistakenly interpreted as either “noise” or a false frequency peak. Spectral decomposition of a signal using PSD reveals a distinct peak of the *dominant frequency* of collagen crimp in the digital image and minimizes erroneous calculations of the crimp period.

2.4.3 Collagen Crimp Analysis

In order to examine possible collagen fiber crimp changes under fatigue, collagen crimp analysis was conducted. In addition to the two uncycled specimens, one cycled specimen in each group and one control specimen were randomly picked and stained for picro Sirius red and permanently prepared under a coverslip. Subsequent polarized light microscopy (Nikon Eclipse Microscope) was performed on each specimen and 5-8

digitized images were recorded at each magnification (e.g. 10x, 20x, and 40x). Collagen crimp analysis, based on the previous work by Hilbert [64], was performed on the digital polarized photomicrographs [65]. Briefly, the images were imported as N (rows) by M (columns) matrices of grayscale pixel intensities into MATLAB® (MathWorks, Inc., Ver. 7.0). The images were then averaged along the columns, creating a vector of averaged intensities having the dimension of 1 (row) by M (columns). This vector was next entered as a discrete intensity versus distance signal into the MATLAB Signal Processing Toolbox®, where a fast Fourier transform (FFT) and power spectral density (PSD) were subsequently performed. Spectral decomposition of a signal using PSD is able to reveal a distinct peak of the dominant frequency of collagen crimp in the digital image.

2.5 Fourier Transform Infrared Spectroscopy (FT-IR) Studies

Infrared spectroscopy is a qualitative technique that obtains information about molecular structure by measuring the frequency of IR radiation needed to excite vibrations in molecular bonds [66]. FT-IR couples the analytical method of infrared spectroscopy with the physical phenomena of total internal reflection (i.e. reflection and refraction of electromagnetic radiation at an interface of two media having different indices of refraction) [66]. Information about the molecular structure of the material, inter- and intra-molecular interactions, crystallinity, protein conformation, and orientation of the molecules can be obtained through analysis of the infrared spectra. FT-IR, which is a nondesctructive technique, was used in this study to assess the molecular changes in collagen Type I (due to denaturation) at each increasing cycle level. The infrared spectra of all proteins indicate that there exists a number of bands characteristic of the peptide bond, and that their positions are sensitive to confirmation

[67]. The amide I band, with characteristic frequencies in the range from 1600 to 1700 $cm^{-1,}$ is widely used for conformational analysis of collagen. It is associated with the stretching vibrations of the peptide carbonyl groups. The collagen amide I band has a complex contour and the shape, position, intensity, and half-width of every component, are greatly dependent on amino acid composition, and sequence of residues in triplets. The multicomponent structure of amide I can be generally attributed to the vibrational interaction between the peptide groups [68]. FTIR testing has been used previously to examine the collagen structure changes at the molecular level for cycled glutaraldehyde treated cross-linked porcine aortic cusps [69]. In this study, the same technique was applied to the cycled GLBP. Both the perpendicular and parallel specimen groups, including controls, were received in distilled water. These tissues were equilibrated in sterile water prior to obtaining FT-IR spectra. The IR spectra (64 scans at 2 cm^{-1} resolution) of specimens in the hydrated state were obtained using Fourier transform IR spectroscopy (FTIR, Jasco 480 Plus) with a fixed 45^{o} angle attenuated total reflectance (ATR, ZnSe) cell attachment. Water was used as a background reference and water spectrum was subtracted from the specimen spectra by the computer program.

2.6 Statistical Analysis

To examine the effects of repeated cycling on the baseline mechanical property changes, comparisons between cyclic loading stops were performed using analysis of variance. Statistically significant difference were concluded when $p<0.05$. All data are represented as the mean SEM (standard error of the mean).

3.0 RESULTS

3.1 Collagen Fiber Architecture Characterization

The width of the I(Φ)versus Φ distribution is indicative of the degree of fiber orientation: highly oriented fiber networks result in a very narrow peak, while less well-oriented fibers yield a broader peak. In the perpendicular specimen group, after $50x10^6$ cycles, the decrease in collagen fiber alignment is indicated by the broader distribution (Figure 32a). In the parallel specimen group, the increase in alignment of collagen fibers is indicated by the narrowing of the R( ) distribution peak (Figure 32b).

As defined previously, the orientation index (OI) is the angle that contains one-half of the total area under the I(Φ)versus Φ distribution. Thus highly oriented fiber networks will have low OI values whereas more randomly oriented networks will have larger values. In the perpendicular specimen group, the OI value increased substantially (p=0.028) from 43.946 0.888 to 48.460 0.300 after $50x10^6$ cycles (Figure 33). The increase in OI corresponds to the fibers becoming less aligned. In the parallel specimen group, there was a substantial (p=0.045) decrease in OI from 49.064 1.898 to 44.413 0.602 after $50x10^6$ cycles. The decrease in OI corresponds to a increase in fiber alignment.

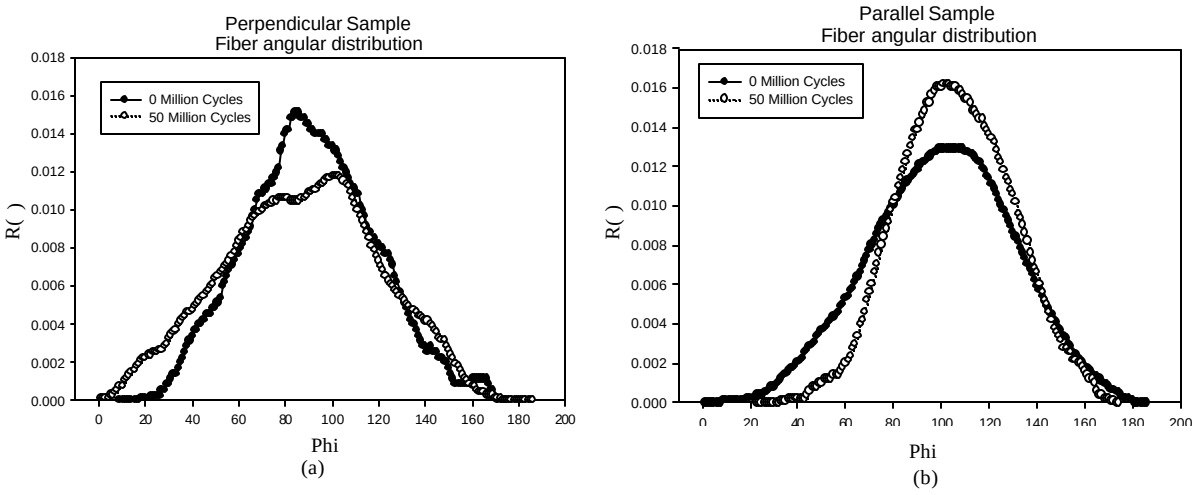

Figure 32 a) In the perpendicular specimen group, after $50x10^6$ cycles the fiber angular distribution R( ) peak broadens which indicates that the fibers are becoming more randomly oriented. b) In the parallel specimen group, the R( ) peak narrows after $50x10^6$ cycles which indicates that the fibers are becoming more aligned.

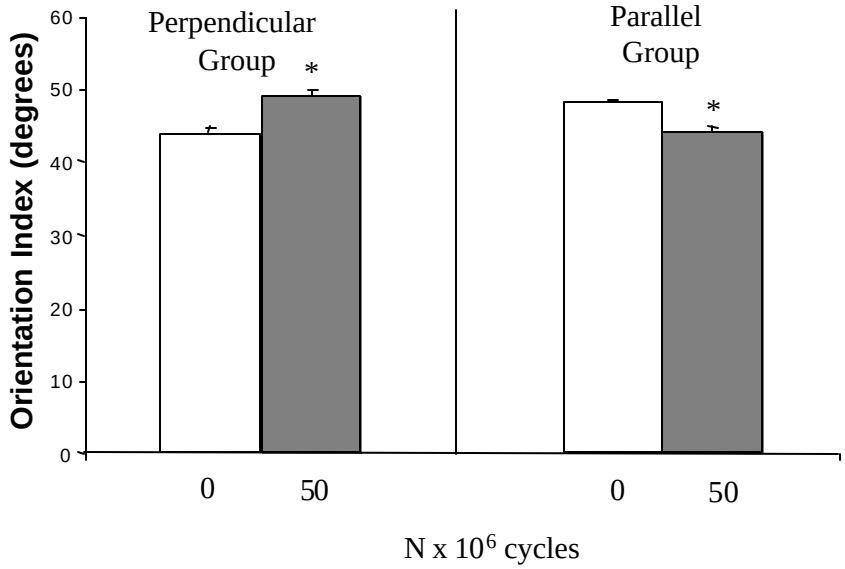

Figure 33 * denotes a statistically significant change. The orientation index increases significantly in the perpendicular specimen group after $50x10^6$ cycles. The increase in OI corresponds to a decrease in fiber alignment. In the parallel specimen group, there was a significant decrease in OI from 49.064 1.898 to 44.413 0.602, after $50x10^6$ cycles, which corresponds to an increase in fiber alignment.

3.2 Permanent Changes in Specimen Geometry with Cycling

As expected, there was a statistically significant permanent set in both specimen groups as evinced by the tissue not returning to its original configuration. In the perpendicular group, there was 5% permanent contraction in the PD after $20x10^6$ cycles ($p= 0.003$) (Figure 34b). After $50x10^6$ cycles, the PD continued to contract and the XD extended substantially from its original state to approximately 17% ($p= 0.002$) (Figure 34b).

In the parallel group, there was a 6% elongation in the PD after $20x10^6$ cycles and virtually no change in the XD. After $50x10^6$ cycles there was a 7% contraction in the XD (Figure 34a). There were no statistically significant changes between $20x10^6$ cycles and $50x10^6$. There were changes for the control group for each cycle level. Also, there were no substantial changes in thickness with cycling (Figure 35).

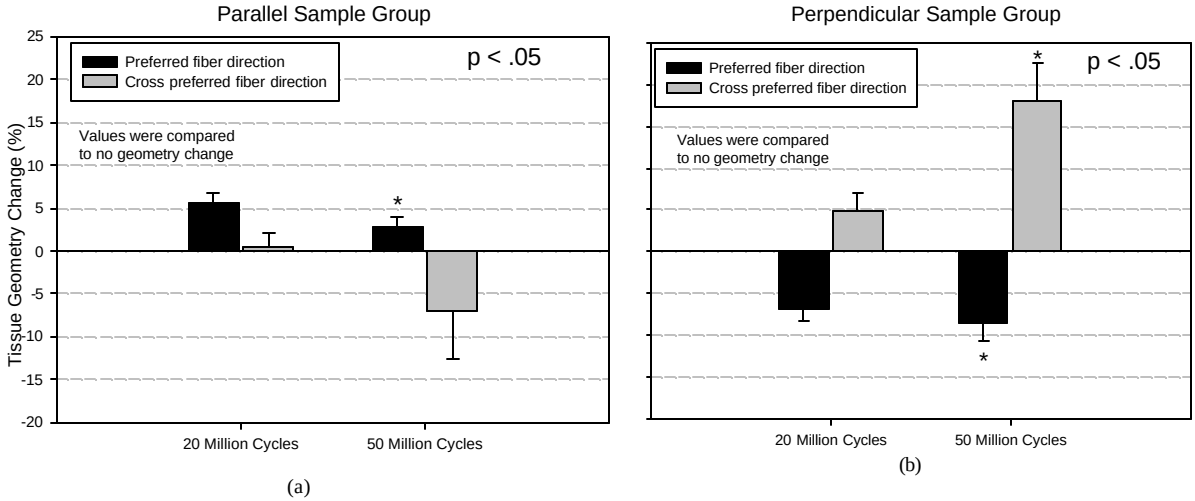

Figure 34 * denotes a statistically significant change. a) In the perpendicular group, there was -5% permanent contraction in the PD after $20x10^6$ cycles. After $50x10^6$ cycles, the PD continued to contract and the XD increased to approximately 17%. b) In the parallel group, there was a 6% increase in the PD after $20x10^6$ cycles and virtually no change in the XD. After $50x10^6$ cycles there was a 7% contraction in the XD.

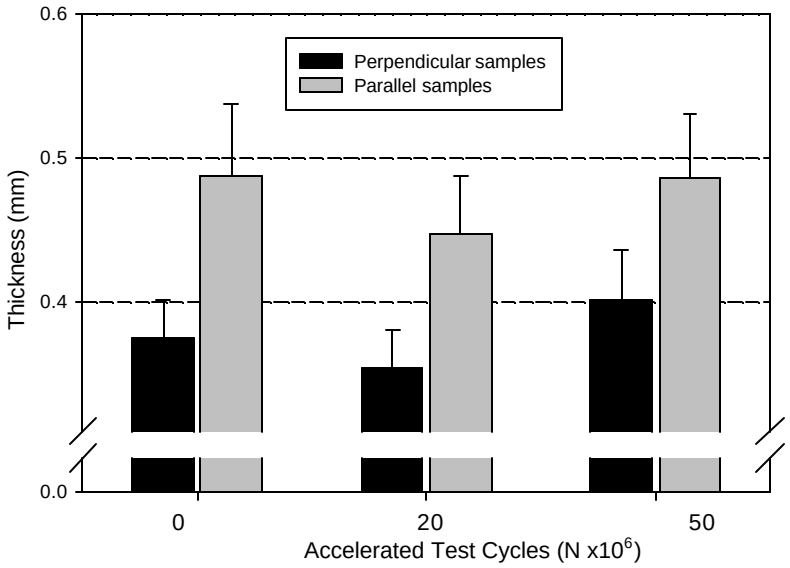

Figure 35 Specimen thickness changes measured at each cycle level. No statistically significant changes were observed.

3.3 Mechanical Property Changes

3.3.1 Referred to the Current State

In Figure 36a, a representative 1st Piola Kirchhoff stress-stretch plot of the perpendicular group shows an increase in the tissue compliance in the PD after $20x10^6$ cycles with a corresponding decrease in compliance after $20x10^6$ cycles in the XD. After $50x10^6$ cycles, the compliance continued to increase in the PD while the compliance did not change appreciably in the XD (as compared to $20x10^6$ cycles). In the perpendicular group, when the biaxial mechanical data were analyzed with respect to the current cycle level, there were statistically significant changes in extensibility only after $20x10^6$

cycles. In the PD, there was a substantial increase in compliance (p=.003) (Figure 37a) with a corresponding decrease in compliance in the XD (p=0.004) (Figure 37b). After $50x10^6$ cycles, the compliance continued to increase in the PD (Figure 37a) (p<0.001) with a corresponding decrease in compliance in the XD (p=0.004) (Figure 37b). A statistically significant increase in the areal stretch at 1 MPa equi-tension occurred after $50x10^6$ cycles (Figure 38).

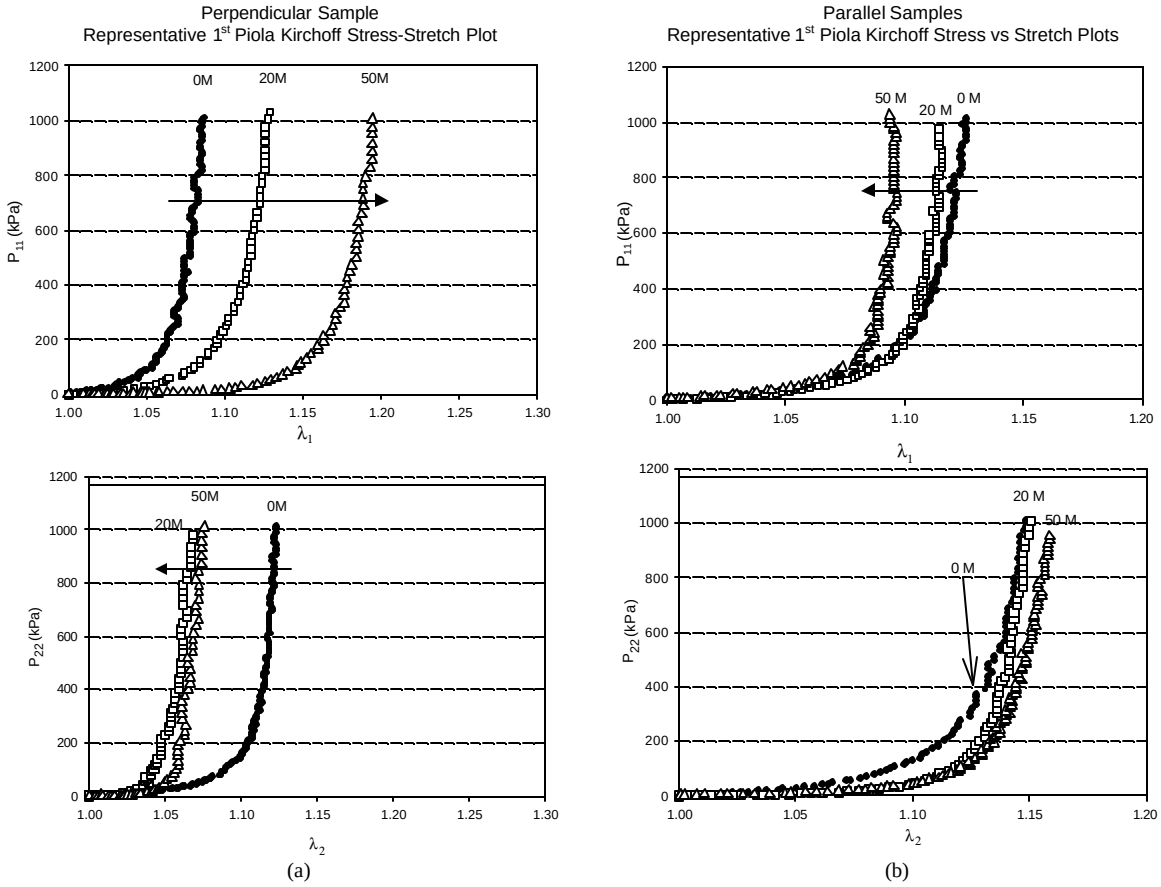

Figure 36 (a) A representative 1st Piola Kirchhoff stress-stretch plot of the perpendicular group showing an increase in the tissues compliance in the PD after $20x10^6$ cycles with a corresponding decrease in compliance after $20x10^6$ cycles in the XD. After $50x10^6$ cycles, the compliance continued to increase in the PD while the compliance did not change appreciably in the XD. (b) A representative 1st Piola Kirchhoff stress-stretch plot of the parallel group showing a decrease in compliance in the PD and a slight increase in compliance in the XD with cycling.

In the parallel group, although slight mechanical property changes were observed, the changes were not as pronounced as the perpendicular group. Representative 1st Piola Kirchhoff stress-stretch plots (Figure 36b) shows a slight decrease in the tissue compliance in the PD (Figure 37a) with cycling and there was virtually no change in the compliance in the XD after $50x10^6$ cycles (Figure 37b). There were no changes in extensibility or areal stretch in the parallel group with cycling (Figure 38).

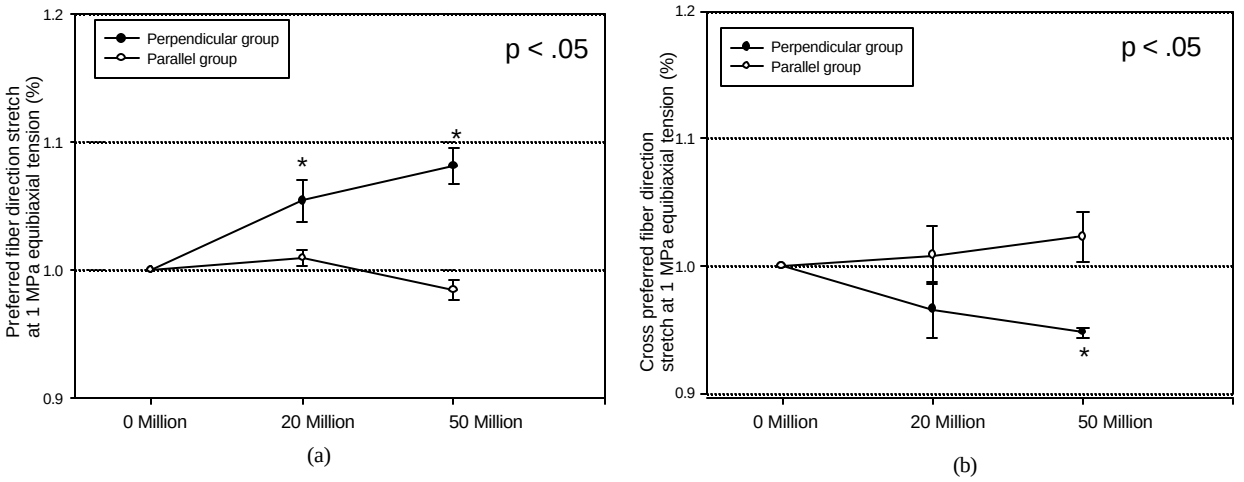

Figure 37 * denotes a statistically significant change**.** Peak stretches in PD and XD that including the effects of preconditioning measured at 1 MPa. For the perpendicular group, there were significant changes in extensibility only after $20x10^6$ cycles when the biaxial strains were referenced to the marker position of current cycle level. In the PD, there was a significant increase in compliance while there was a corresponding significant decrease compliance in XD. After $50x10^6$ cycles, the compliance continued to increase in the PD with a corresponding decrease in compliance in the XD. In the parallel group, there were no significant changes in extensibility with cycling.

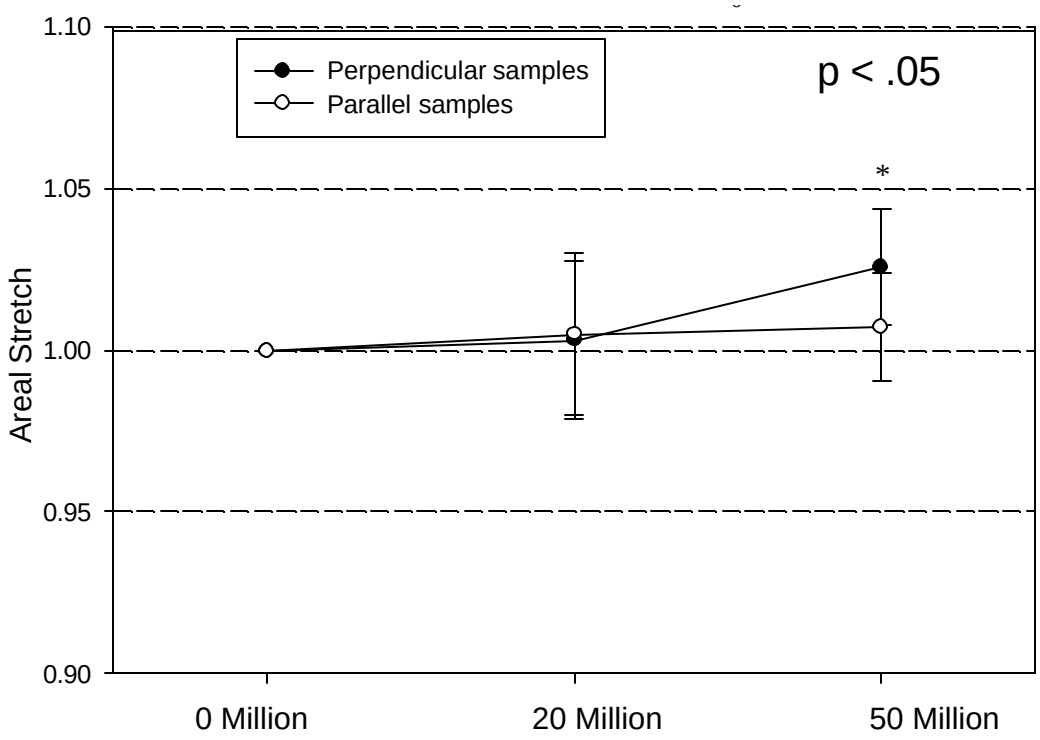

Figure 38 * denotes a statistically significant change. Significant changes were only measured after $50x10^6$ cycles in the perpendicular specimen group when the areal stretch is referenced to the current state.

3.3.2 Referred to the Uncycled State

In the perpendicular specimen group, there was a significant increase in areal stretch after $50x10^6$ cycles ($p= 0.016$) (Figure 39). In the parallel specimen group, there was a significant decrease after $50x10^6$ cycles ($p<0.05$) (Figure 39).

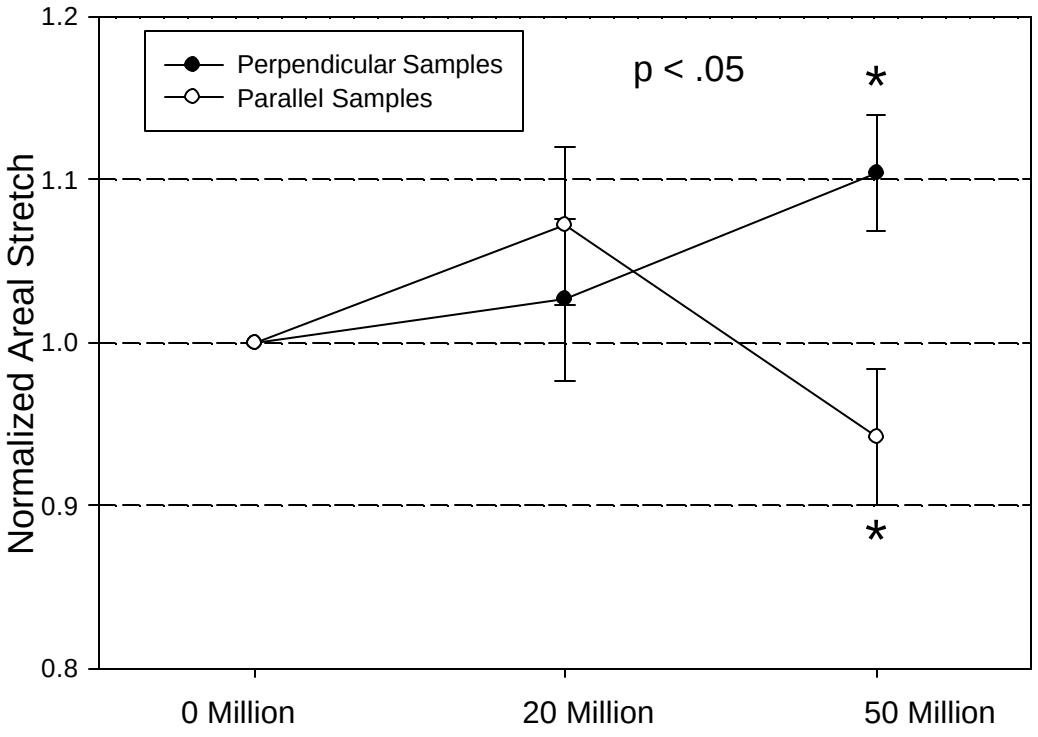

Figure 39 In the perpendicular group, when the biaxial strains were referenced to the uncycled state and the effects of preconditioning are included, a) there was significant increase in areal stretch after $50x10^6$ cycles ($p=0.006$). In the parallel group, there is a statistically significant decrease in the areal stretch.

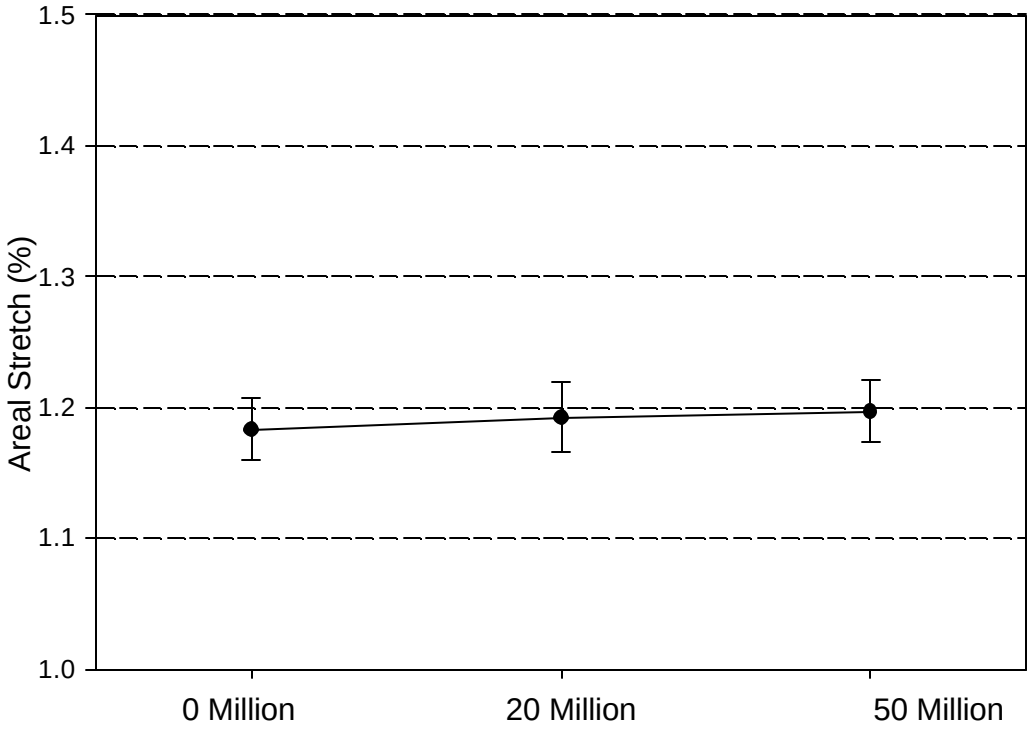

Figure 40 There were no statistical changes in areal stretch in the control group.

3.4 Quantification of Collagen Fiber Crimp Morphology

In the perpendicular specimen group, at 0x10^6 cycles, collagen fiber crimp was measured at 23.46 1.39 m. Although there was a slight increase in collagen fiber crimp at the 50x10^6 cycle level, there were no changes in the collagen fiber crimp period after 50x10^6 cycles (Figure 41). In the parallel specimen group, collagen crimp period increased substantially after 20x10^6 cycles ($p=0.023$) from 23.46 1.389 m to 28.14 0.84 m. The collagen crimp period continued to substantially when compared to the uncycled collagen crimp after 50x10^6 cycles resulting in a crimp period of 29.00 0.62 m ($p=0.010$) (Figure 41).

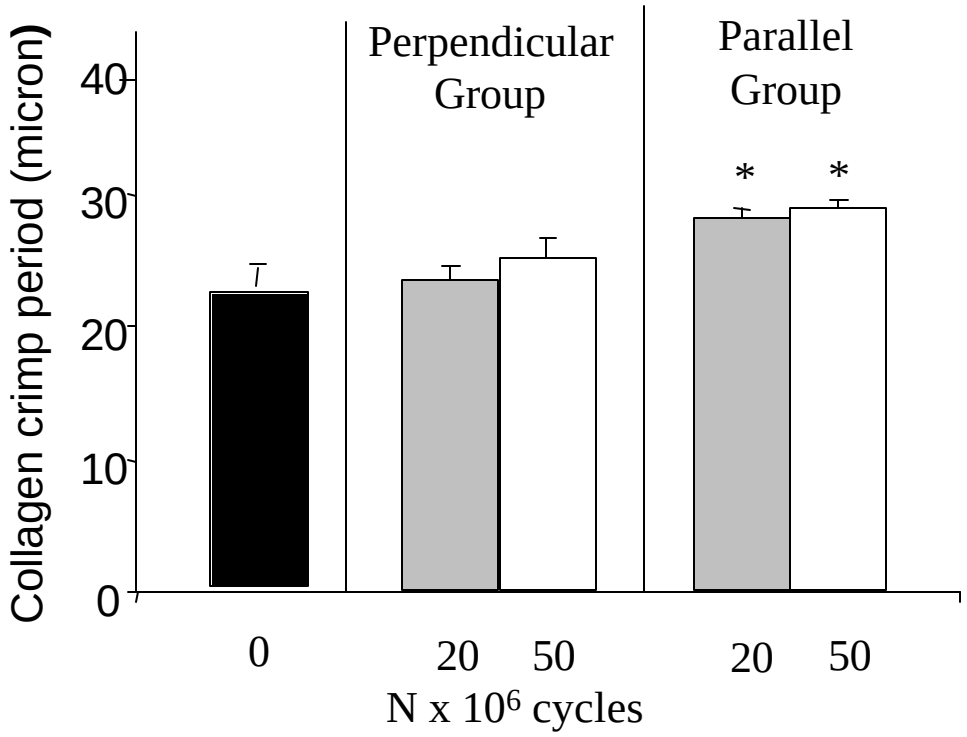

Figure 41 * indicates statistically different from 0 cycles. Changes in crimp period with cycling in the parallel and perpendicular groups. In the perpendicular specimen group, there were no changes in collagen fiber crimp period after $50x10^6$ cycles, although there was a slight, but not significant increase in collagen fiber crimp at the $50x10^6$ cycle level. In the parallel group, collagen crimp period increased approximately by 20% after only $20x10^6$ cycles and continued to increase significantly at $50x10^6$ cycles resulting in an overall increase of collagen crimp period of 24%.

3.5 FTIR Results

Representative specimens from each group were assessed for protein conformational changes by ATR-FTIR spectroscopy. Both groups showed typical spectrum for Type I collagen, the major protein in the pericardium (Figure 43 a). Two major peaks were found, one at 1660-1630 (Amide I peak from C=O stretching vibrations) and other at 1553 cm-1 (Amide II peak for amide N-H bending vibrations coupled with C-N stretching). Amide I peak at 1660-1630 cm-1 was separated into three

peaks, viz. 1651, 1642, and 1632 cm^{-1} showing carbonyls in different environments. After $20x10^6$ cycles, both the parallel and perpendicular groups showed significant changes in the amide I region suggesting collagen denaturation. The peaks at 1651 and 1642 cm^{-1} were reduced in intensity and the peak at 1632 cm^{-1} was increased in the intensity. There were no differences between the perpendicular specimen group and the parallel specimen group (Figure 42). After 50 million cycles, no further changes in the FTIR peaks were noted for any specimens suggesting that collagen denaturation takes place by 20 million cycles with no further changes in collagen spectra after additional cycling of pericardium. There was consistent increase in the peaks at 1079 cm^{-1} and 1031 cm^{-1} in all cycled specimens as compared to controls. All other peaks in cycled specimens were similar to that of control specimens.

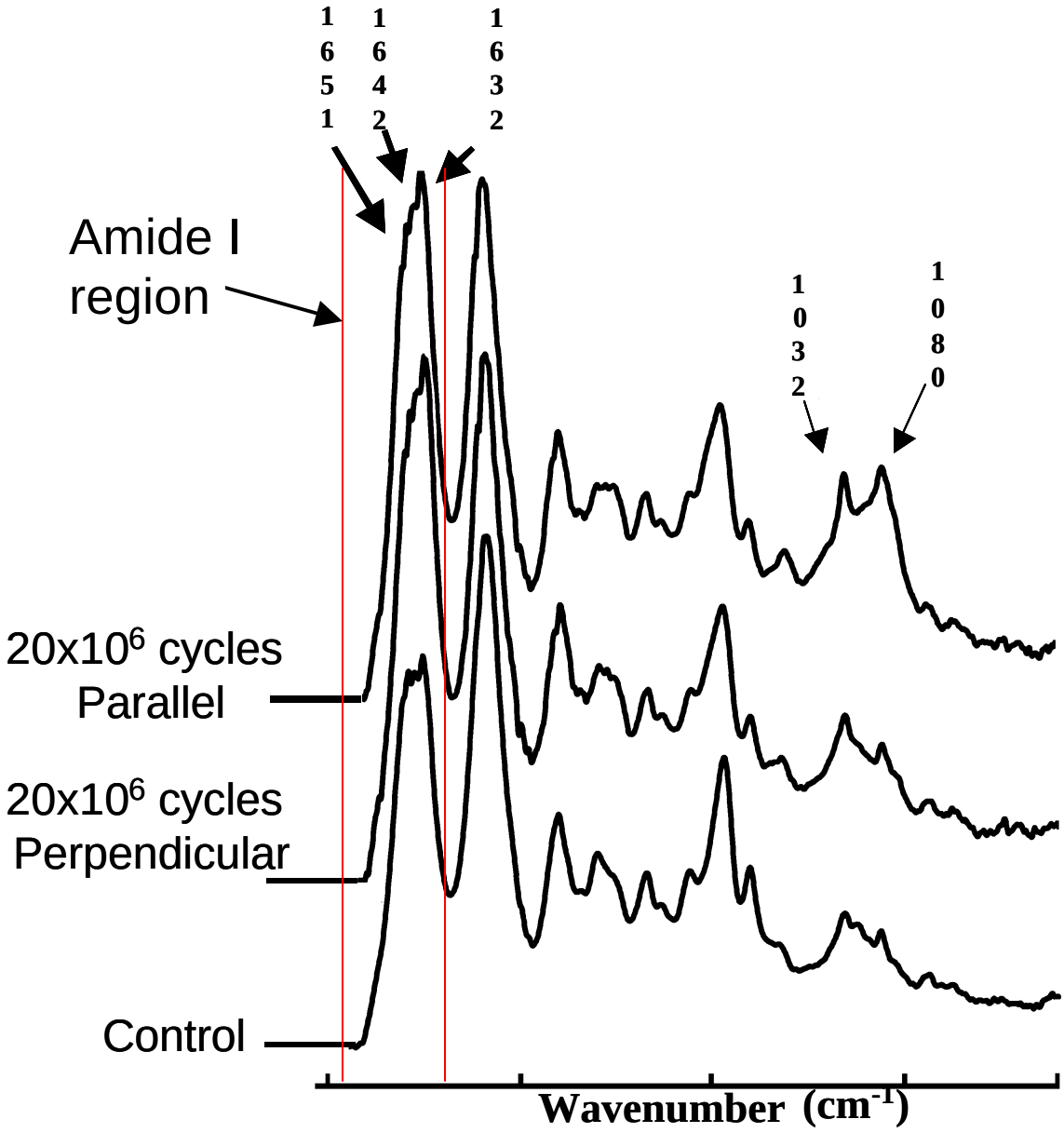

Figure 42 FT-IR spectra for control specimens, 20 million cycled perpendicular specimens and 20 million cycled parallel specimens. Amide I peak (in between the two red lines) at 1660-1630 cm-1 was separated into three peaks, viz. 1651, 1642, and 1632 cm^{-1} showing carbonyls in different environments. After $20x10^6$ cycles, both the perpendicular and parallel groups showed significant changes in the amide I region suggesting collagen denaturation. The peaks at 1651 and 1642 cm^{-1} were reduced in intensity and the peak at 1632 cm^{-1} was increased in the intensity. There were no differences between the perpendicular specimen group and the parallel specimen group.

4.0 DISCUSSION

4.1 Possible Mechanisms for Mechanical Behavior Changes due to Repeated Cyclic Loading

When mechanical properties of a collagenous tissue are altered when subjected to tensile-only cyclic loading, two possible underlying mechanisms may be at work: 1) the intrinsic properties of the collagen fibers are changed, possibly due to collagen molecule conformation change and denaturation or damage and 2) the collagen fiber network architecture is altered due to a spatial arrangement of collagen fiber architecture (fiber un-crimping and reorientation).

Table 1 summarizes the major findings in the parallel specimen group. In the parallel specimen group, the changes observed can be explained in part by both fiber reorientation and fiber un-crimping. As the tissue is cycled, the collagen fibers un-crimp in the direction of loading which causes the tissue to become stiffer in the PD when biaxial strains were referenced to the marker position of current cycle level. In addition to fiber un-crimping, with repeated cycling, the collagen fibers reorient toward the direction of loading [70] [41], which results in a stiffening in the PD. During cycling loading, as the collagen fibers rotate toward the direction of loading (i.e. the PD axis) and become more aligned, less fibers are oriented in the XD causing an increase in compliance in the XD (Figure 43). When the strain data was referenced to the initial, uncycled state there was a significant decrease in areal stretch at 50×10^6 cycles. This indicates that the intrinsic properties of collagen have been altered with repeated cyclic loading. The overall tissue behavior of the tissue stiffened with cycling.

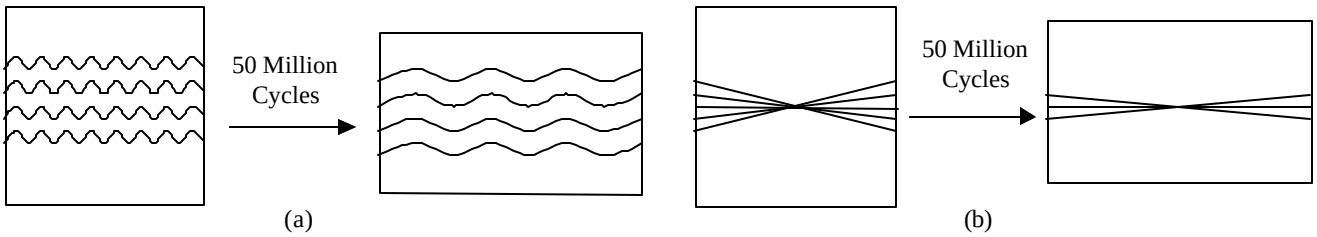

Figure 43 Schematic showing the changes the parallel specimen group collagen fibers underwent as a result of cycling loading. In (a), after $20x10^6$ cycles, the collagen crimp period increased and in (b) after $50x10^6$ cycles the fibers in the rotated towards the direction of loading thus resulting in a more highly aligned fiber network.

Table 1 Summary of major results for the parallel specimen group.

Methods	Results
SALS	Increase in overall fiber alignment
Permanent Set Effects	Elongation in PD
	Contraction in XPD
Mechanical Property Changes:	Substantial increase in compliance in PD
referenced to current state of $50x10^6$ cycles	Substantial decrease in compliance in PD
Mechanical Property Changes:	Substantial decrease in compliance
referenced to uncycled state	
Collagen fiber crimp	Substantial increase in collagen fiber crimp period
FT-IR	Collagen conformational changes after $20x10^6$ cycles

Table 2 lists the major findings in the perpendicular specimen group. Since there were no collagen crimp changes in the perpendicular group, fiber reorientation plays a major role in explaining the mechanical property changes when the biaxial strains were referenced to the marker position of current cycle level. Similar to the parallel specimen group, the only difference being that the axes are switched, the XPD became stiffer because the collagen fibers reoriented towards the direction of the load (Figure 44). Simultaneously, the PD became less stiff due to the tendency of the collagen fibers to reorient towards the direction of loading thus leaving fewer fibers in the PD to bear load. As for the mechanical changes observed in the perpendicular group when referenced to the uncycled state, these results are not as straightforward.

The significant increase in areal stretch at $50x10^6$ cycles is an indicator of intrinsic property changes of collagen. The increase in overall tissue compliance could be due to damage. If the repeated cycling induced micro cracks in the collagen fibers, the resulting stresses

Table 2 Summary of major results for the perpendicular specimen group.

Methods	Results
SALS	Decrease in overall fiber alignment
Permanent Set Effects	Contraction in PD
	Elongation in XPD
Mechanical Property Changes:	Substantial increase in compliance in PD
referenced to current state of $50x10^6$ cycles	Substantial decrease in compliance in PD
Mechanical Property Changes:	Substantial increase in compliance
referenced to uncycled state	
Collagen fiber crimp	No change
FT-IR	Collagen conformational changes after $20x10^6$ cycles

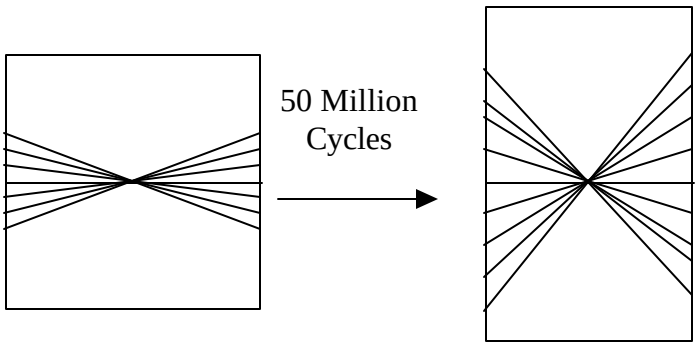

Figure 44 Schematic showing how the XD collagen fibers in the perpendicular specimen group reoriented towards the direction of the load.

and thus the compliance would increase. Another option would be that the increase in compliance is due not to the collagen fibers themselves but to the breaking of the lateral bonds between the collagen. If the lateral bonds are broken due to repeated cyclic loading, the tissue would become more extensible. However, to fully validate this hypothesis, transmission electron microscopy must be performed.

Glutaraldehyde fixation introduces a large number of stable crosslinks between the amino acid groups of the polypeptide chains of collagen [71]. It has been assumed that the collagen fiber architecture and the corresponding mechanical behavior are locked in place when chemically fixed with glutaraldehyde. Further, the mechanical properties of the valve are assumed to remain unchanged during valve operation. Previous work in our laboratory with intact porcine BHV that under went in-vitro accelerated tests cycles indicated that the chemically treated collagenous network did undergo architectural changes that resulted in mechanical property changes not associated with damage [52]. With this in mind, when considering the results of this study, it is evident that chemical fixation with glutaraldehyde does not lock the collagen fibers in place but rather that the collagen fiber architecture is irreversibly altered after only $20x10^6$ cycles. Depolymerization and repolymerization of the glutaraldehyde crosslinks in the deformed configuration may also help explain the permanent set effects observed.

4.2 Collagen Conformational Changes

Infrared spectroscopy has been used extensively to study protein conformation. In particular, infrared spectrum of Type I collagen has been thoroughly investigated [67, 68, 72-75] [75]. The amide I carbonyl stretching region (1700-1600 cm^{-1}) has been shown to be very sensitive to the changes in collagen's triple helical tertiary structure during fibrillogenesis and denaturation [68] [74, 75]. The amide I peak is made up of

three distinct bands; a band at 1651 cm^{-1} is assigned to the carbonyls that are within the triple helix, which are associated intra-molecularly with weaker hydrogen bonds. A band at 1642 cm^{-1} is assigned to the solvent hydrogen bonded glycine residues in the triple helix and a band at 1632 cm^{-1} is assigned to amide carbonyls protruding out from the triple helix and are associated inter-molecularly with water molecules [74, 75]. Thus, increase in the intensity of 1632 cm^{-1} band as compared to the 1651 cm^{-1} as observed after $20x10^6$ cycles suggest that cyclic fatigue of pericardial tissue leads to collagen conformational changes and denaturation probably due to changes in helicity caused by mechanically induced molecular fatigue. Similar increases in the intensity of peak at 1630 cm^{-1} for collagen to gelatin transitions has been reported for pure Type I collagen [75]. In our laboratory we have recently shown that such denaturation of collagen bundles occur at 65 million cycles. In this study we looked at whether orientation during cyclic fatigue has any role in extent of collagen denaturation. Our results suggest that cycling in either orientation parallel or perpendicular to collagen bundles did not change the extent of collagen denaturation as assessed by FTIR spectroscopy. Moreover, FTIR spectra of $20x10^6$ cycles were similar to the specimens cycled for $50x10^6$ cycles suggesting that collagen denaturation takes place early in the fatigue experiments. We have also shown similar collagen denaturation occurring after cyclic fatigue of BHV fabricated from glut crosslinked porcine aortic cusps [69]. In those experiments we have shown that glycosaminoglycans (GAGs) present in the tissue leach out very early (after 10 million cycles) [69]. Thus, it may be possible that GAGs present in the pericardial tissue in this study may have leached out early in the fatigue experiments thus allowing collagen denaturation to take place. This speculation is supported by the FTIR spectra of all cycled specimens, where consistent increase in the peaks at 1079 cm^{-1} and 1031 cm^{-1} were seen after fatigue (Figure 43). Similar changes in the FTIR spectra were seen in our previous study after cyclic fatigue of glutaraldehyde crosslinked porcine bioprosthetic heart valve tissues [69]. In this region (1100-800 cm-1), FTIR spectral peaks are complex and occur due to several overlapping bending vibrations. Thus, precise identification of GAG peaks in this area is not possible.

Thus, overall infrared spectroscopy studies suggest that cyclic fatigue of bovine pericardium causes collagen denaturation after $20x10^6$ cycles with no further changes with additional cycling. The orientation of specimen during fatigue seems to have no effect on collagen denaturation.

4.3 Limitations

Throughout the study there were no problems attributed to the design of the device itself with exception of the enlargement of holes where the pins were inserted during mounting of the specimens. The enlargement of the holes can probably be attributed to the number of pins that are used. A more adequate stress distribution could be achieved if more pins were utilized. Also, using larger specimens would ensure a homogenous strain distribution if the specimens need to be to trimmed due to hole enlargement. A load cell shorted during the study. Fortunately, the short occurred near the $20x10^6$ cycle level and the specimen was sacrificed for histology. All of the other load cells maintained their calibration load readings to ±0.01 kg-f of their original readings performed at the end of the study. Also, in future studies the stress level should be lowered to simulate more physiological loading conditions. An appropriate stress level that has been estimated in BHV using FEM simulations is ~300 kPa [55] [54].

The accuracy of repetitive tissue deformation measurements at each cycle level is dependent on the integrity of the optical markers glued on the central region of the specimens. After 50×10^6 cycles, optical markers stayed on all cycled specimens and five control specimens, suggesting the feasibility of using optical marker for strain measurement in tissue fatigue study.

SALS testing should have been performed at $20x10^6$ cycles. However, in the interest of minimizing down time between cycle stop levels, SALS testing was not performed at the $20x10^6$ cycles level in this study. SALS data at this cycle level would

help elucidate whether the mechanical property changes at that point were only results of fiber un-crimping or were a combination of collagen fiber un-crimping and fiber reorientation.

As for histology, specimens should have also been cut in the XD so that the changes in fiber crimp in the XD could be determined. Also, transmission electron microscopy should have been performed to determine if the lateral bonds between the collagen molecules were broken in some areas.

4.4 Implications for Future Studies

Most importantly, the present study reinforces the concept that the long-term durability of a tissue valve is extraordinarily dependent on the ongoing quality of its extracellular matrix, especially collagen [4]. Once the mechanisms of damage are understood, they can be utilized in the design of novel chemical and mechanical treatments and other conditions of valve fabrication that seek to enhance collagen stability and reduce the flexural stresses implicated in degradation of the collagenous matrix. Ensuring that loading and unloading of the valve does not occur perpendicular to the preferred fiber direction is an example of how valve design could impact the durability of the BHV. Since fatigue-induced structural damage will continue to be a major factor in the durability of virtually all types of tissue valves, the mechanisms of tissue valve collagen deterioration clearly warrant further study. The principles derived from this study and future studies should serve to guide future valve design and development of novel chemical treatments that minimize the findings in this study and future studies which.

The next phase of this work would be to develop a structural constitutive model based on the experimental data generated in this study. Structural constitutive models

attempt to integrate information on tissue composition and structure to avoid ambiguities in material characterization, and offer insight into the function, structure, and mechanics of tissue components. Structural constitutive models have been developed for a variety of intact tissues and tissue components including lung [76], collagen [77] [78], cartilage [79], passive myocardium [80], heart valves [50], and maturing skin [81]. Previously, we have developed a similar structural approach for chemically treated pericardial tissues [82]. However, in that study only a two-parameter exponential stress-strain law was used; neither a $R(\theta)$ sensitivity analysis nor histological validation studies were performed. In a subsequent study in our lab, fiber orientation information obtained using small angle light scattering (SALS) was directly incorporated into a structural constitutive model based on work by Lanir [39, 83]. In that study, an alternate recruitment function stress-strain law provided insight into tissue function. Using the structural model developed in that study, it was found that at the maximum Green-Lagrange strain level of 0.16 used in that study, results for the cumulative distribution function $F(\varepsilon)$, which represents the fraction of fibers of the total that are stretched at the current strain level, indicated that only ~22% of the collagen fibers are fully straightened. These results indicate that even at peak tissue stresses of up to 300 kPa, bovine pericardium still has a substantial structural reserve. This result is not surprising since that native pericardium is known to fail at stresses of ~20 MPa [84] [85]. Thus the ability of the structural model to predict these types of finding clearly indicate that implementation of a structural model is warranted.

5.0 SUMMARY

Changes in BHV subjected to repeated cyclic loading are manifested at the molecular, fiber and tissue level. Kinematic rearrangement and intrinsic property changes of the collagen fibers occurred in both groups. Profound changes were observed in the mechanical properties and irreversible changes occurred in the collagen fiber architecture after only $20x10^6$ cycles. The primary result of this study suggests that BHV biomaterials fatigue response is highly sensitive to fiber orientation with respect to the direction of loading. Specifically, when the cyclic loading is perpendicular to the PD, fiber reorientation is the dominant mechanism in mechanical property changes. In contrast, when the cyclic loading is parallel to the PD, both collagen fiber crimp and collagen fiber reorientation occur. Taken as a whole, the results of this study suggest that 1) collagen orientation plays a critical role in BHV fatigue response, and 2) chemical fixation technologies that allow greater fiber mobility under functional stresses yet without permanent set effects may yield more durable materials.

BIBLIOGRAPHY

1. Fung, Y.C., *Biodynamics:circulation*. 1984, New York: Springer-Verlag. 404.

2. Thubrikar, M., *The Aortic Valve*. 1990, Boca Raton: CRC. 221.

3. Schoen, F.J., *Future directions in tissue heart valves: impact of recent insights from biology and pathology*. J Heart Valve Dis, 1999. **8**(4): p. 350-8.

4. Schoen, F. and R. Levy, *Tissue heart valves: Current challenges and future research perspectives*. Journal of Biomedical Materials Research, 1999. **47**: p. 439-465.

5. Schoen, F.D. and C.E. Hobson, *Anatomic analysis of removed prosthetic heart valves: causes of failure of 33 mechanical valves and 58 bioprostheses, 1980-1983*. Human Pathology, 1985. **16**: p. 545-549.

6. Gross, L. and M. Kugel, *Topographic anatomy and histology of the valves in the human heart*. American Journal of Pathology, 1931. **7**: p. 445-456.

7. Ionescu, M.I., et al., *Clinical durability of the pericardial xenograft:11 years experience*, in *Cardiac Bioprostheses*, L.H. Cohn and V. Gallucci, Editors. 1982, Yorke Medical Books: New York. p. 709-717.

8. Ishihara, T., et al., *Structure and Classification of Cuspal Tears and Perforations in Porcine Bioprosthetic Cardiac Valves Implanted in Patients*. The American Journal of Cardiology, 1981. **48**: p. 665-678.

9. Schoen, F. and R. Levy, *Pathology of Substitute Heart Valves*. Journal of Cardiac Surgery, 1994. **9**: p. 222-227.

10. Schoen, F.J., *Pathology of heart valve substitution with mechanical and tissue prostheses*, in *Cardiovascular Pathology*, M.D. Silver, A.I. Gotlieb, and F.J. Schoen, Editors. 2001, Livingstone: New York.

11. Turina, J., et al., *Cardiac bioprostheses in the 1990s*. Circulation, 1993. **88**(2): p. 775-81.

12. Elkins, R., *Surgery for valvular heart disease*. Curr Opin Cardiol, 1990. **5**(2): p. 199-208.

13. Schoen, F.J., *Cardiac valve prostheses: pathological and bioengineering considerations*. J Card Surg, 1987. **2**(1): p. 65-108.

14. Schoen, F.J., *Cardiac valve prostheses: review of clinical status and contemporary biomaterials issues*. J Biomed Mater Res, 1987. **21**(A1 Suppl): p. 91-117.

15. Sacks, M.S. and F.J. Schoen, *Collagen fiber disruption occurs independent of calcification in clinically explanted bioprosthetic heart valves.* J Biomed Mater Res, 2002. **62**(3): p. 359-71.

16. Vesely, I., J.E. Barber, and N.B. Ratliff, *Tissue damage and calcification may be independent mechanisms of bioprosthetic heart valve failure.* J Heart Valve Dis, 2001. **10**(4): p. 471-7.

17. Love J.W., P.W. Willems, and C.S. Love, *New Horizons and the future of heart valve prostheses*, ed. S. Gabbay and F. R.W. 1994, Austin: Silent Partners.

18. Brown JC and T. R., *The collagen superfamily.* Int Arch Allergy Immunol, 1995. **107**(4): p. 484-90.

19. Baum and Brodsky, *Folding of peptide models of collagen and misfolding in disease.* Current Opinion in Structural Biology, 1999. **9**: p. 122-128.

20. Voet and Voet, *Biochemistry*. 1995, John Wiley and Sons.

21. Silver, F.H., *Biological Materials: Structure, Mechanical Properties, and Modeling of Soft Tissues*. 1987, New York and London: New York University Press.

22. Kastelic, J. and E. Baer, *Deformation of Tendon Collagen*, in *The Mechanical Properties of Biological Materials*, J.F. Vincient and J.D. Currey, Editors. 1980, Society for Experimental Biology: Great Britain. p. 397-433.

23. Ramachandran, G.N., *Chemistry of collagen.*, in *Treatise on collagen*, Ramachandran, Editor. 1967, Academic Press: NY.

24. Fung, Y.C., *Biomechanics: Mechanical Properties of Living Tissues*. 2nd ed. 1993, New York: Springer Verlag. 568.

25. Bornstein and Byers, *Current concepts- collagen metabolism*. 1980: Scope Publications.

26. Nimni, M.E. and R.D. Harkness, *Molecular structure and functions of collagens.*, in *Collagen Volume I Biochemistry.*, M.E. Nimni, Editor. 1988, CRC Press: Boca Raton, FL.

27. Silver, F.H., K.H. Langley, and R.L. Trelstad, *Type I collagen fibrillogenesis: initiation via reversible linear and lateral growth steps.* Biopolymers, 1979. **18**: p. 2523.

28. Prockop and Fertala, *The Collagen Fibril:The Almost Crystalline Structure. y.* Journal of Structural Biolog, 1998. **122**: p. 111-118.

29. Hodge, A.J. and J.A. Petruska, *Recent studies with the electron microscope on ordered aggregates of the tropocollagen molecule*. Aspects of Protein Chemistry. Vol. 289-300. 1963, London: Academic Press.

30. Kadler, et al., *Collagen fibril formation.* Biochemistry Journal, 1996. **316**: p. 1-11.

31. Bella, et al., *Crystal and Molecular Structure of a Collagen like peptide at 1.9 angstrom resolution.* Science, 1994. **266**: p. 75-81.

32. Ottani, V., M. Raspanti, and A. Ruggeri, *Collagen strucutre and functional implications.* Micron, 2001. **32**: p. 251-260.

33. Ottani, O., et al., *Collagen fibrillar networks as skeletal frameworks: a demonstration by cell-maceration/scanning electron microscope method.* Arch Histol Cytol, 1988. **51**(3): p. 249-61.

34. Gordon, J.E., Royal Society of London, 1970. **319**: p. 137.

35. Hukins, D.W.L., *Collagen Orientation*, in *Connective Tissue Matrix*, D.W.L. Hukins, Editor. 1984, Verlag,Chemie. p. 211-240.

36. Viidik, A., *Interdependence between Structure and Function in Collagenous Tissues*, in *Biology of Collagen*, Viidik and Vuust, Editors. 1980, Academic Press: London.

37. Fung, Y.C., *Elasticity of soft tissues in simple elongation.* Am J Physiol, 1967. **213**(6): p. 1532-44.

38. Diamant and e. al, *Collagen; ultrastructure and its relation to mechanical properties as a function of aging.* Proc R Soc Lond B, 1972. **180**: p. 293-315.

39. Sacks, M.S., *A structural constitutive model for planar collagenous tissues that integrates SALS-derived fiber orientation data.* Journal of Biomechanial Engineering, in-press.

40. Waldman, S.D., M.S. Sacks, and J.M. Lee, *Boundary conditions during biaxial testing of planar connective tissues: Part 2: Fiber orientation.* J. Materials Science: Materials in Medicine, 2002. **in-press**.

41. Billiar, K.L. and M.S. Sacks, *A method to quantify the fiber kinematics of planar tissues under biaxial stretch.* J Biomech, 1997. **30**(7): p. 753-6.

42. Dale, W.C. and E. Baer, *Fiber buckling in composite systems: a model for the ultrastructure of uncalcified collagen tissues.* J. Material Science, 1974. **9**: p. 369-382.

43. Bellows, C.G., A.H. Melcher, and J.E. Aubin, *and organization of collagen gels by cells cultured from the periodontal ligament, gingival, and bone suggest functional differences between cell types.* J Cell Sci, 1981. **50**: p. 299-314.

44. Gathercole, L.J. and A. Keller, *Crimp morphology in the fibre-forming collagens.* Matrix, 1991. **11**: p. 214-234.

45. Trowbridge, E.A. and C.E. Crofts, *Pericardial Heterograft valves: An assessment of leaflet stresses and their implications for heart valve design.* Journal of Biomedical Engineering, 1987. **9**: p. 345-355.

46. Gordon, J.E., *The science and structure of materials.*, in *The science and structure of materials.* 1988, Freeman: New York.

47. Reifsnider, K., ed. *Fatigue of Composite Materials*. Composite Materials Series. Vol. 4. 1991, Elsevier: Amsterdam. 715.

48. Sacks, M.S. and C.J. Chuong, *Orthotropic mechanical properties of chemically treated bovine pericardium.* Ann Biomed Eng, 1998. **26**(5): p. 892-902.

49. Sacks, M.S., D.B. Smith, and E.D. Hiester, *A small angle light scattering device for planar connective tissue microstructural analysis.* Ann Biomed Eng, 1997. **25**(4): p. 678-89.

50. Billiar, K.L. and M.S. Sacks, *Biaxial mechanical properties of fresh and glutaraldehyde treated porcine aortic valve cusps: Part II - A structurally guided constitutive model.* Journal of Biomechanical Engineering, 2000. **122**(4): p. 327-335.

51. Sacks, M.S., *Biaxial mechanical evaluation of planar biological materials.* Journal of Elasticity, 2000. **61**: p. 199-246.

52. Wells, S.M. and M.S. Sacks, *Effects of fixation pressure on the biaxial mechanical behavior of porcine bioprosthetic heart valves with long-term cyclic loading.* Biomaterials, 2002. **23**(11): p. 2389-99.

53. Hildebrand, D., et al., *A novel testing system for fatigue studies of heart valve biomaterials.* Ann Biomed Eng, submitted.

54. Black, M.M., et al., *A Three-dimensional Analysis of a Bioprosthetic Heart Valve.* Journal of Biomechanics, 1991. **24**: p. 793-801.

55. Krucinski, S., et al., *Numerical Simulation of Leaflet Flexure in Bioprosthetic Valves Mounted on Rigid and Expansile stents.* Journal of Biomechanics, 1993. **26**: p. 929-943.

56. Downs, J., et al., *An Improved Video-based Computer Tracking System for Soft biomaterials Testing.* IEEE Transactions on Biomedical Engineering, 1990. **37**: p. 903-907.

57. Humphrey, J., D. Vawter, and R. Vito, *Quantification of Strains in Biaxially Tested Soft Tissues.* Journal of Biomechanics, 1987. **20**(1): p. 59-65.

58. Hoffman, A.H. and P. Grigg, *A Method for Measuring Strains in Soft Tissue.* Journal of Biomechanics, 1984. **10**: p. 795-800.

59. Bathe, K.J., *Finite Elements Proceedures in Engineering Analysis*. 1982, Englewood Cliffs,NJ: Prentice-Hall.

60. Humphrey, J.D., D.L. Vawter, and R.P. Vito, *Quantification of Strains in Biaxially Tested Soft tissues.* Journal of Biomechanics, 1987. **20**: p. 59-65.

61. Montes, G.S. and L.U. Junqueira, *Histochemical localization of collagen and of proteoglycans in tissues*, in *Collagen Volume II*, M.E. Nimni, Editor. 1988, CRC Press: Boca Raton, FL.

62. Brigham, E.O., *The Fast Fourier Transform and Its Applications*. 1988, Englewood Cliffs, NJ: Prentice-Hall, Inc. 488.

63. Hilbert, S.L., V.J. Ferrans, and W.M. Swanson, *Optical methods for the nondestructive evaluation of collagen morphology in bioprosthetic heart valves.* Journal of Biomedical Materials Research, 1986. **20**: p. 1411-1421.

64. Hilbert, S., et al., *Simultaneous assessment of bioprosthetic heart valve biomechanical properties and collagen crimp length.* Journal of Biomedical Materials Research, 1996. **31**: p. 503-509.

65. Fulchiero, G., et al., *Alterations in Collagen Fiber Crimp morphology with Cyclic Loading in Zero and Low Pressure-Fixed porcine bioprosthetic heart valves.* Biomaterials, submitted.

66. Merrett K, et al., J Biomater Sci Polym Ed, 2002. **13**(6): p. 593-621.

67. Doyle, B.B., E.G. Bendit, and E.R. Blout, *Infrared spectroscopy of collagen and collagen-like polypeptides.* Biopolymers, 1975. **14**(5): p. 937-57.

68. Lazarev, Y.A., B.A. Grishkovsky, and T.B. Khromova, *Amide I band of IR spectrum and structure of collagen and related polypeptides.* Biopolymers, 1985. **24**(8): p. 1449-78.

69. Vyavahare, N., et al., *Mechanisms of bioprosthetic heart valve failure: fatigue causes collagen denaturation and glycosaminoglycan loss.* J Biomed Mater Res, 1999. **46**(1): p. 44-50.

70. Broom, N.D., *The Stress-Strain and Fatigue Behavior of Glutaraldehyde Preserved Heart-Valve Tissue.* Journal of Biomechanics, 1977. **10**: p. 707-724.

71. Bowes, A. and C.W. Cater, *The Interaction of Aldehydes with Collagen.* Biochimica et Biophysica Acta, 1968. **168**: p. 341-352.

72. Susi, H., J.S. Ard, and R.J. Carroll, *The infrared spectrum and water binding of collagen as a function of relative humidity.* Biopolymers, 1971. **10**(9): p. 1597-604.

73. Jakobsen, R.J., et al., *Intermolecular interactions in collagen self-assembly as revealed by Fourier transform infrared spectroscopy.* Science, 1983. **220**(4603): p. 1288-90.

74. Payne, K.J. and A. Veis, *Fourier transform IR spectroscopy of collagen and gelatin solutions: deconvolution of the amide I band for conformational studies.* Biopolymers, 1988. **27**(11): p. 1749-60.

75. George, A. and A. Veis, *FTIRS in H2O demonstrates that collagen monomers undergo a conformational transition prior to thermal self-assembly in vitro.* Biochemistry, 1991. **30**(9): p. 2372-7.

76. Mijailovich, S.M., D. Stamenovic, and J.J. Fredberg, *Toward a kinetic theory of connective tissue micromechanics.* J Appl Physiol, 1993. **74**(2): p. 665-81.

77. Comninou, M. and I.V. Yannas, *Dependence of Stress-Strain Nonlinearity of Connective Tissues on the Geometry of Collagen Fibers.* Journal of Biomechanics, 1976. **9**: p. 427-433.

78. Buckley, C.P., D.W. Lloyd, and M. Konopasek, *On the deformation of slender filaments with planar crimp: theory,numerical solution and applications to tendon collagen and textile materials.* Proceedings of the Royal Society of London, 1980. **A 372**: p. 33-64.

79. Farquhar, T., P.R. Dawson, and P.A. Torzilli, *A microstructural model for the anisotropic drained stiffness of articular cartilage.* J Biomech Eng, 1990. **112**(4): p. 414-25.

80. Horowitz, A., et al., *Structural Three Dimensional Constitutive Law for the Passive Myocardium.* Journal of Biomechanical Engineering, 1988. **110**: p. 200-207.

81. Belkoff, S.M. and R.C. Haut, *A structural model used to evaluate the changing microstructure of maturing rat skin.* J Biomech, 1991. **24**(8): p. 711-20.

82. Sacks, M.S., *A structural constitutive model for chemically treated planar connective tissues under biaxial loading.* Computational Mechanics, 2000. **26**(3): p. 243-249.

83. Lanir, Y., *Constitutive Equations for Fibrous Connective Tissues.* journal of biomechanics, 1983. **16**: p. 1-12.

84. Zioupos, P. and J.C. Barbenel, *Mechanics of Native Bovine Pericardium: I. The multiangular behavior of strength and stiffness of the tissue.* Biomaterials, 1994. **15**: p. 366-373.

85. Lee, J.M., M. Ku, and S.A. Haberer, *The bovine pericardial xenograft: III - Effect of uniaxial and sequential biaxial stress during fixation on the tensile viscoelastic properties of bovine pericardium.* Journal of Biomedical Materials Research, 1989. **23**: p. 491-506.